Designing a System for Measuring and Optimizing the Photothermal Conversion Efficiencies of Two Dimensional Nanomaterials for Cancer Therapy

by

Darren Ted Juin Chang

A thesis
presented to the University of Waterloo
in fulfillment of the
thesis requirement for the degree of
Master of Applied Science
in
Mechanical and Mechatronics Engineering (Nanotechnology)

Waterloo, Ontario, Canada, 2021

Author's Declaration

I hereby declare that I am the sole author of this thesis. This is a true copy of the thesis, including any required final revisions, as accepted by my examiners.

I understand that my thesis may be made electronically available to the public.

Abstract

Cancer is a devastating disease with no definitive cure currently. Current treatments are invasive and can cause inreprepable damage to the human body. Alternative cancer treatment methods involving nanomaterials have been sought primarily for their ability to treat cancer non-invasively. This is accomplished in a variety of ways and combinations of treatments such as photothermal therapy, photodynamic therapy and drug delivery. In this thesis, the photothermal properties of tungsten and molybdenum compounds are studied for prospective use in photothermal therapy cancer treatments.

A femtosecond laser is used to alter the morphology, stoichiometry and chemistry of the tungsten disulfide (WS_2) and molybdenum disulfide (MoS_2) starting materials. This resulted in a novel synthesis method for creating two dimensional (2D) tungsten semi-carbide (W_2C) through carburizing WS_2 and synthesizing plasmonic substoichiometric molybdenum oxide (MoO_{3-x}) through the partial oxidation of MoS_2. These novel nanomaterials were then characterized using grazing incidence x-ray diffraction (GIXRD), scanning electron microscopy (SEM), x-ray photoelectron spectroscopy (XPS), atomic force microscopy (AFM) and Raman spectroscopy to confirm the corresponding carburization and partial oxidation.

Optical and photothermal studies were conducted to determine the feasibility of these materials as a photothermal agent used in photothermal therapy. Absorption spectroscopy was used to study the materials' interaction with light, specifically in the near infrared (NIR) wavelengths. A custom measurement system was designed and engineered to measure the photothermal conversion efficiency (PTCE) of both the 2D W_2C and the plasmonic MoO_{3-x}. The PTCE was

measured to be 27% and 33% for the 2D W_2C and the plasmonic MoO_{3-x}, respectively. This suggests both materials are strong candidates as a photothermal agent for use in photothermal therapy.

This novel synthesis method of both two dimensional 2D W_2C and the plasmonic MoO_{3-x} utilizes a femtosecond laser and creates unique nanomaterials which exhibit strong photothermal heating at a NIR wavelength. In comparison to the WS_2 and MoS_2 starting materials, the PTCE was significantly improved, suggesting a promising clinical use for an alternative non-invasive treatment to cancer.

Acknowledgements

First, I would like to acknowledge my supervisor Kevin Mussleman for his continuous support in my studies and research. He has given me advice and guidance throughout my journey and is always willing to listen to my ideas.

Second, I would also like to thank PhD student Fan Ye who has helped me complete a significant portion of my research. Much of my research would be incomplete without his expertise and hard work. Thank you for being an amazing friend.

Third, I would like to thank my friends and research group members for making my MASc an enjoyable experience.

Finally, and most importantly I would like to thank my family who have provided unconditional support throughout my academic journey. Without them I would not be where I am today.

Dedication

I dedicate this work to my late grandmother (婆婆) who passed away from cancer. Thank you for always believing in us! We are one step closer to finding a cure.

Table of Contents

List of Figures

List of Tables

List of Abbreviations

WS_2	Tungsten Disulfide
WO_3	Tungsten Oxide
MoS_2	Molybdenum Disulfide
MoO_{3-x}	Substoichiometric Molybdenum Oxide
MoO_3	Molybdenum Oxide
H_xMoO_3	Hydrogen Bonded Molybdenum Oxide
Ti_3AlC_2	Titanium Aluminum Carbide
W_2C	Tungsten Semi-carbide
WC	Tungsten Carbide
BN	Boron Nitride
2D	Two Dimensional
3D	Three Dimensional
SEM	Scanning Electron Microscopy
XPS	X-ray Photoelectron Spectroscopy
AFM	Atomic Force Microscopy
NIR	Near Infrared
PTCE	Photothermal Conversion Efficiency
HOMO	Highest Occupied Molecular Orbital
LUMO	Lowest Unoccupied Molecular Orbital
EDX	Energy-dispersive X-ray
JCPDS	Joint Committee on Powder Diffraction Standards
TMO	Transition Metal Oxide
LSPR	Localized Surface Plasmon Resonance

UV-vis	Ultraviolet-visible
FWHM	Full Width at Half Max
CAD	Computer Aided Model

Chapter 1 Introduction

1.1 What is Cancer?

Cancer is defined as a collection of diseases which involves uncontrolled, abnormal cellular growth with the potential to spread to various parts of the human body [1]. The cause of these diseases occurs when the body is no longer able to control the cells from rapidly dividing. Normally, most cells in the body have a finite lifespan, however when the older cells continuously grow and form new abnormal cells that do not die, a clump of extra cells which is referred to as a tumor is formed. The body is unable to maintain homeostasis which ultimately leads to fatality if left untreated. This collection of diseases causes an estimated 10 million fatalities annually worldwide [2] and is the leading cause of death in Canada resulting in approximately 30% [2] of deaths in Canada per year. Reasons for such a devastatingly high mortality rate can be attributed to the fact that cancer can originate from anywhere within the body. However in men, the most common type of cancer originates from the prostate and in women the most common cancer is found in the breast tissue [2]. The complexity in properly treating cancer stems from the fact that there are over 100 different types of cancers [2] in addition to new types being discovered continuously. Each type of cancer has unique properties and characteristics that can make one treatment effective against it while making another one completely ineffective.

1.2 Current Cancer Treatments

Presently, there are three main forms of treatments generally accepted by most medical professionals which are surgical removal, chemotherapy and radiation therapy. Each has their own benefits and drawbacks and is used with the intention of killing as many cancerous cells while leaving the normal healthy cells intact. However, these treatments are still considered

invasive because all cells are targeted in a general area in order to destroy the majority of cancer cells. Depending on the classification, type and stage of the cancer, different treatments are used often in conjunction to accomplish the task of eliminating cancer cells while keeping the patient healthy. However, a promising and upcoming treatment involving nanoparticles is being developed for the battle against cancer. More specifically, a technique known as photothermal therapy has been proposed to destroy cancer cells while keeping the remaining normal cells healthy.

1.2.1 Surgical Removal

The oldest procedure involves surgically removing the cancerous tissue alongside any nearby tissues. This is usually with the intention of either diagnosing or removing the tumors. If the goal is to diagnose and stage the cancer, then a medical procedure known as a biopsy is performed in which a surgeon will make an incision to the suspected area of interest and remove the suspicious tissue usually with a sharp syringe needle for further study [1]. Oftentimes this method is used in combination with other cancer treatments such as chemotherapy or radiation therapy if the cancer cells are aggressive and have started to spread to other parts of the body. Usually some form of medical imaging is used in combination with the excisional tool to ensure accuracy and precision during the removal of the tissue. Ultrasound is the most common medical imaging tool used to guide surgeons and map out the location of the tumor cells. Magnetic resonance imaging (MRI) can also be utilized to help provide spatial resolution throughout the area of interest [1]. However, ultrasound is more often utilized during real time surgeries whereas MRIs only provide a high resolution snapshot of the operable area. Although an effective method to remove tumors, there are many drawbacks which give rise to alternative methods of cancer treatment. The main drawback being the size of the tumor such that a tumor being too large or

too small can make the surgical procedure very difficult with a high risk of damaging vital healthy tissue [1].

1.2.2 Chemotherapy

Cancer cells that have the tendency to divide and spread very rapidly are often ideal subjects for chemotherapy. The basic principle of chemotherapy involves using a concoction of drugs in order to disrupt the cell division process to stop cancer cells from growing and dividing. Like the surgical removal of tumors, chemotherapy may be used in combination with other cancer treatments in order to have a more effective impact. Chemotherapy is most effective in targeting cells throughout the body as the drugs travel through the bloodstream allowing effectiveness anywhere in the body [1]. Although generally grouped as one technique, chemotherapy falls into many different classes depending on the mechanism. Oftentimes, multiple classes of chemotherapy are utilized in combination to reduce the recurrence and prevent cancer cells from being resistant to the effects of the drugs. Depending on the class of chemotherapy used, different points in the cell cycle would be targeted which can allow a wider variety of effectiveness compared to targeting a single point during the cell cycle [1]. Variability aids in preventing cancer cells from adapting to the drugs and allows for a more successful treatment plan.

Although a very powerful and effective technique used to treat many different types of cancers, chemotherapy can be very dangerous as there is currently no way for the drugs to differentiate between healthy cells and cancer cells. Hence, many of the healthy cells are at risk of being severely damaged in the process of undergoing chemotherapy. The harsh concoction of highly damaging drugs induce many negative short term side effects in patients such as nausea,

vomiting or diarrhea as well as many long term effects such as hair loss and infertility [1]. The short and long term list of side effects is almost never ending which incentivizes researchers to seek out better solutions requiring less severe side effects.

1.2.3 Radiation Therapy

Radiation can be found almost anywhere due to the wave-particle properties of matter. The energy from the movement of particles or waves from electrons and photons can be utilized in many medical applications. More specifically, when radiation is produced artificially by machines, the energy from the x-rays can be used to view snapshots of the human body. Usually, the doses for x-rays are very minimal and can be considered relatively safe. However, these lower doses of radiation can be increased to much higher doses in order to damage cancer cells and shrink tumors. Like chemotherapy, the goal of radiation therapy is to damage the DNA in cancer cells beyond repair such that the cancer cells are unable to divide or grow. Usually, radiation therapy is paired with other cancer treatments such as chemotherapy due to the radiation targeting one area of the body. Radiation therapy is best suited to preventing cancer cells from returning once destroyed or making the tumor less aggressive [1]. There are generally two main types of radiation therapies which are external and internal beam therapy [1].

External beam radiation therapy involves high dose radiation from a machine that aims an x-ray source at the localized tumor area. There is no physical contact between the machine and the patient, however multiple beams of radiation irradiate the specified area. Medical imaging modalities such as an MRI or CT scan will be implemented to map out the tumor location to ensure accuracy in the radiation beam.

Internal radiation therapy involves injecting a source of radiation directly at the source of the tumor in order to slowly damage the DNA of the tumor cells. Also known as brachytherapy, internal radiation therapy involves inserting a sealed capsule containing a radioactive substance into the tumor site [1]. Usually higher doses of radiation can be given with this type of treatment compared to external beam radiation because the radiation is much more localized.

Like chemotherapy, radiation therapy has many unwanted side effects such as fertility problems or osteoporosis, however there is a higher probability of getting another cancerous tumor in the future due to the elevated amounts of radiation which can damage DNA in such a way that uncontrolled cell division may occur.

1.3 What is Photothermal Therapy?

An upcoming and promising new cancer treatment technique known as photothermal therapy allows for the utilization of nanoparticles in combination with laser optics to treat cancer. As the name suggests, photothermal means the conversion of light into heat, more specifically utilizing the properties of nanosize particles to achieve an efficient method of converting light into heat. The central dogma for this technique involves utilizing the conversion of light energy into thermal energy in order to target cancerous cells, as portrayed in Figure 1.1. Heating body tissue to temperatures above 40°C is shown to be effective in damaging and killing cancer cells while leaving the surrounding healthy tissue relatively healthy as opposed to the cancer treatments mentioned before [3]. Various nanomaterials such as gold nanorods have been shown to achieve controlled temperatures well above the 40°C threshold through converting light at a specific wavelength to vibrational (heat) energy, demonstrating the use of nanoparticles as a promising candidate for photothermal therapy [4].

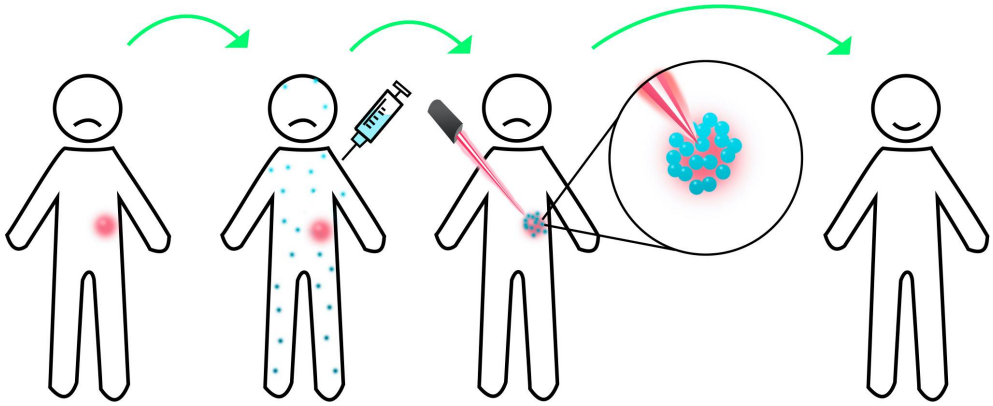

Figure 1.1 An overview of photothermal therapy. Patient is injected with nanoparticles. Nanoparticles gather into the tumor. Patient is irradiated with a NIR laser. Nanoparticles absorb the laser's energy generating heat. Tumor is destroyed by heat.

1.4 Thesis Overview

Chapter 2 will discuss important properties of nanomaterials which contribute to the feasibility of use as a photothermal agent used in photothermal therapy. This chapter will also outline the current state of the art in photothermal agents and explain the photothermal mechanisms found in most nanomaterials.The most important metric to determining a nanomaterial's viability as a photothermal agent is known as the photothermal conversion efficiency, which is also introduced in Chapter 2. It corresponds to the amount of heat energy generated by the photothermal agent, per light energy absorbed by the agent. Chapter 3 will discuss the system involved in measuring and calculating the photothermal conversion efficiency as well as the calibration and accuracy of this measurement method. Chapter 4 will explore the photothermal properties of molybdenum oxide nanomaterials synthesized using a femtosecond laser. Chapter 5 will focus on the synthesis and characterization of tungsten semi-carbide nanomaterials, as synthesized by a femtosecond laser. The photothermal properties of the tungsten semi-carbide nanomaterials will be discussed in this chapter as well. Finally, Chapter 6 will conclude by explaining possible improvements to the PTCE measurement techniques, as well as areas for future work.

Chapter 2 Literature Review

2.1 What Makes a Good Photothermal Agent?

Ideally, photothermal agents should have a high photothermal conversion efficiency (PTCE), good photostability, high tumor uptake and strong absorption in either the near infrared (NIR) I or II biological windows. The ultimate goal of photothermal agents is to be able to penetrate or contact the tumorous cells and induce hyperthermia by converting light energy to heat. This is usually done with intravenous injection of the nanomaterials which gradually accumulates into the tumor through the enhanced permeability and retention effect (EPR) shown in Figure 2.1. The EPR effect is a phenomenon in which molecules of certain sizes (100 to 200 nm) will accumulate in higher concentrations in cancer cells in comparison to normal cells due to the numerous fenestrations only found commonly in the blood vessels of tumors [5]. The theory behind this phenomenon is rooted in the fact that tumour cells grow and divide much more rapidly compared to healthy cells which indicates the need for a higher volume of blood supply. This is known as cancer angiogenesis in which tumour cells become dependent on the constant creation of new blood vessels to support the growth of the tumour cells. However, the newly formed blood vessels are highly abnormal and exhibit properties and structures differing from normal blood vessels. Tumour blood vessels are very chaotically structured; they have weak associations between endothelial cells, lack smooth muscle cells and have poor lymphatic drainage which leads to the direct passageway of certain sized particles reaching the tumour site.

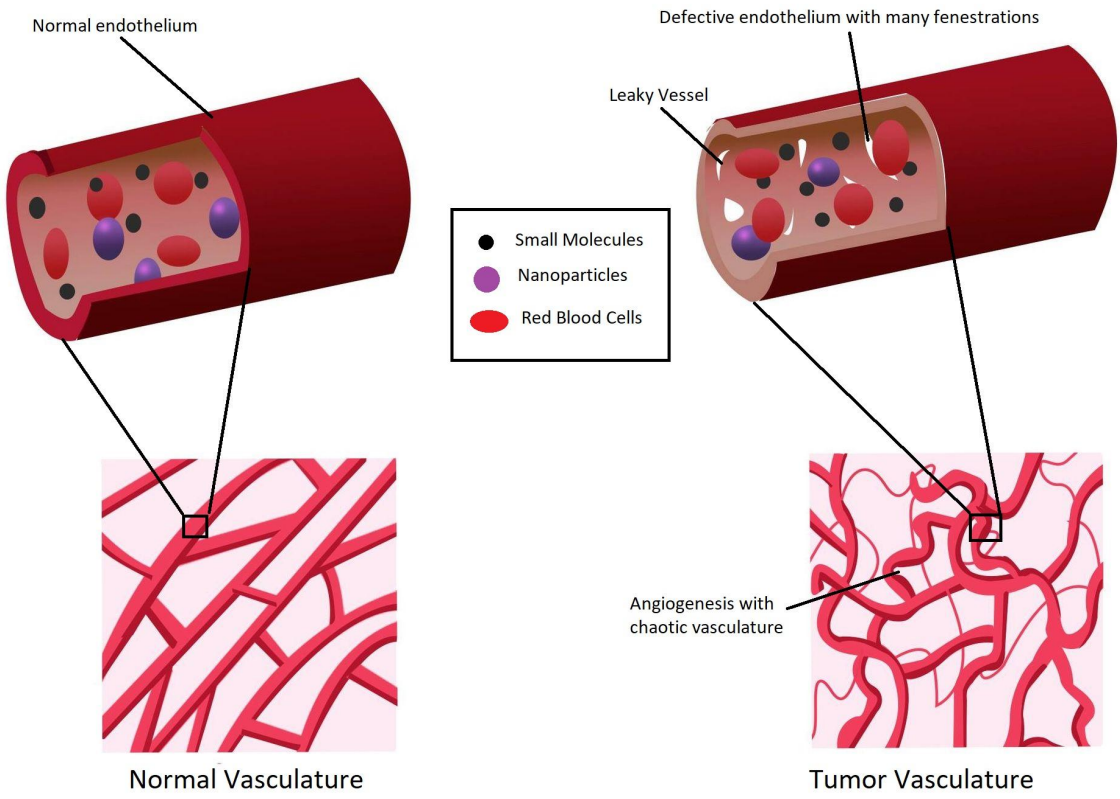

Figure 2.1 Comparison between normal vasculature and tumor vasculature. Leaky vasculature allows nanoparticles to enter freely into tumor cells.

Once homogeneously absorbed by the tumor cells, the nanomaterials are then irradiated by infrared light. The effectiveness of this is highly dependent on the nanomaterials ability to absorb the incoming light. Hence the near infrared spectrum is chosen as the irradiating light in order to avoid absorbance from biological components such as blood, water, collagen and proteins. The wavelengths between 700-900 nm and 1000-1400 nm correspond to the NIR-I and NIR-II wavelength ranges respectively [6]. The nanomaterials ability to absorb light in the NIR wavelengths and the PTCE, will affect how much light is converted into heat. In most cases, heating tumor tissue above 40°C will induce tumor death via necrosis. Many factors play into

this as the irradiation wavelength and power density must be chosen carefully to allow for maximum penetration and light conversion. Wavelengths between the NIR-I and NIR-II range are typically absorbed by red blood cells, hence only the specific wavelengths are chosen for the NIR-I and NIR-II regions in which NIR light is able to penetrate with minimal interference [6].

In addition to strong NIR absorption and PTCE, photothermal agents may also exude certain attributes which can affect tumor accumulation and penetration. The two main attributes which can be considered are a nanomaterial's size and shape.

Blood clearance of nanomaterials is highly size dependent, indicating that some nanomaterials may not reach the intended tumor target due to the incorrect size. Nanomaterials that are in between 3-5 nm are too small and tend to be cleared quickly via renal filtration which is undesirable for tumor accumulation [7]. In addition, nanomaterials with larger diameters greater than 200 nm tend to accumulate in the liver and spleen without reaching the target tumor [8]. Thus, with these restrictions, the optimal size for the EPR effect to occur is between 100-200 nm [8]. Wang et al. had attached polyethylene glycol (PEG) to MoS_2 nanosheets and observed that the nanosheets between 80 and 100 nm had better tumor uptake in comparison to 300 nm nanosheets [9].

The shape of the nanomaterial also has a significant impact on tumor accumulation and penetration. However these properties may vary depending on which nanomaterials are chosen, for example, Tang et al. coated Palladium nanosheets with silica which changed the shape of the Palladium from 2D nanosheets to a nanosphere. This transition in shape increased the cellular uptake from tumor cells by an astounding 13 times [10].

Good photostability is also an important factor when selecting suitable photothermal agents. Degradation through light exposure, oxidation or biological exposure is undesirable for nanomaterials. Equally important, nanomaterials subjected to NIR light irradiation must be able to continuously convert NIR light into heat without degradation. Usually to test for photostability, nanomaterials are subjected to NIR light in cycles of irradiation and non irradiation. The temperature should increase proportionally to the irradiation cycles and should be consistent.

Overall, an ideal photothermal agent is able to absorb NIR light that is minimally absorbed by organic tissues found in the human body. In addition, the photothermal agent should demonstrate a high PTCE indicating that a significant amount of the absorbed irradiating light energy is converted into heat. Moreover, the photothermal agent has good photostability when irradiated by NIR light indicating minimal degradation. Finally, it was found that the best nanomaterial size for optimal tumor uptake via the EPR effect is in between 100-200 nm [8].

2.2 Previously Reported Photothermal Agents

Currently there are countless studies of photothermal agents being researched, however the focus of this work is two dimensional (2D) nanomaterials. In this chapter, several types of photothermal agents will be discussed including transition metal dichalcogenides (TMD), MXenes and graphene/graphene oxide (GO). These 2D nanomaterial classes are the most commonly studied materials for 2D photothermal agents and provide a good background on the state of the art for 2D photothermal agents.

Graphene oxide (GO) consists of layers of sp^2 carbons bonded together containing oxygen functional groups. GO has been previously reported as a good photothermal agent due to the intrinsically high absorption in the NIR range. Yang et al. injected PEGylated nano-GO (nGO-PEG) in mice and were able to demonstrate high passive tumour accumulation via the EPR effect and were effectively able to destroy the tumor cells with an 808 nm laser [11]. Due to graphene and GO having a large surface area, there is great potential in synergistic cancer drug treatments along with photothermal therapy. There are delocalized p-electrons on the graphene plane which allow for bonding to aromatic molecules via π-π bonds such as camptothecin (CPT) [12] and doxorubicin (DOX) [13]. Moreover, Savchuk et al. measured the PTCE of both graphene and GO at 808 nm to be an astounding 67% and 58% [14] respectively. Both graphene and GO demonstrate high NIR absorbance, good EPR effect, a large surface area for functionalization and PTCE values well above 50%, showing promising photothermal properties for photothermal therapy.

Transition Metal Dichalcogenides (TMD) are another class of 2D nanomaterials similar in structure to graphene, however they differ in electronic properties. Chemically, a TMD consists of a hexagonal 2D layer of a transition metal (M) sandwiched between two layers of chalcogen atoms (X) which produces the MX_2 stoichiometry as seen in Figure 2.2. These sandwiched layers are held together by a weak van der Waals force, allowing simple methods to create monolayers from bulk material. As a semiconducting material, a TMD has sizable bandgaps, high carrier mobility and good stability in air [15]. Moreover, TMDs have strong NIR absorbance which has prompted great interest in exploring the photothermal effects of TMDs in photothermal therapy. The photothermal effects of both WS_2 and MoS_2 have been extensively studied showing PTCE values in the ranges of 13-40% [16],[17],[18] and 24-55% [19],[20],[21] respectively. The

variability in the ranges of PTCE values can be mainly attributed to the different synthesis methods involving different functional groups (bovine serum albumin = BSA, folic acid = FA and polyethylene glycol = PEG) and different morphologies (nanosheets, nanoflakes, nanospheres and quantum dots). In addition to photothermal therapy, both WS_2 and MoS_2 have been used in syngestic cancer treatments involving photoacoustic imaging [16], radiation therapy [18] and chemotherapy/drug loading [21], demonstrating the value of TMDs in nanomedicine.

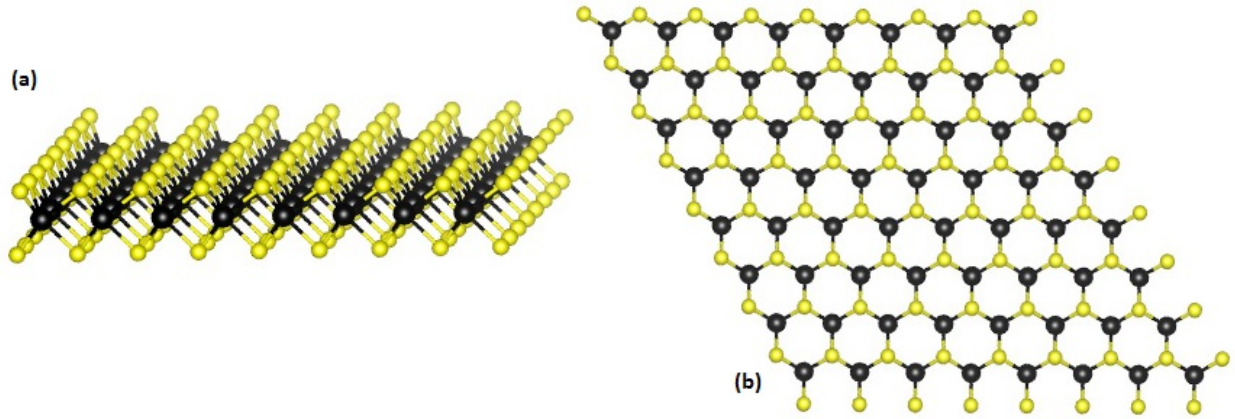

Figure 2.2 (a) Side view and (b) Top view of transition metal dichalcogenides. The metal M is shown in black and the dichalcogenide X is shown in yellow [87] "Crystal structure of a monolayer of transition metal dichalcogenide" by 3113Ian is licenced under CC BY-SA 3.0

MXenes are a class of transition metal carbides and nitrides in which a unique top down etching method is used to synthesize these 2D nanomaterials. Typically, MXenes are synthesized by selectively etching the A layer found in the $M_{n+1}AX_n$ phase in which M is the transition metal, X is either carbon or nitrogen and A is a group IIIA or IVA element [22]. Figure 2.3 illustrates the typical etching process involved in creating MXenes. The thickness of MXenes is typically in the nanometer range while the lateral dimension is in the micrometer range which demonstrates the 2D nature of this material [23]. The synthesis method allows for simple surface functionalization of functional groups such as oxygen, hydroxyl or fluorine [24]. Numerous MXene nanomaterials have been studied and have stated excellent photothermal performances, namely from Ti_3C_2,

Nb_2C and Ta_4C_3. The PTCE values from Ti_3C_2, Nb_2C and Ta_4C_3 were 30% [25], 38% [26] and 45% [27] respectively. MXenes also have excellent absorption in the NIR range [28] for use in photothermal therapy.

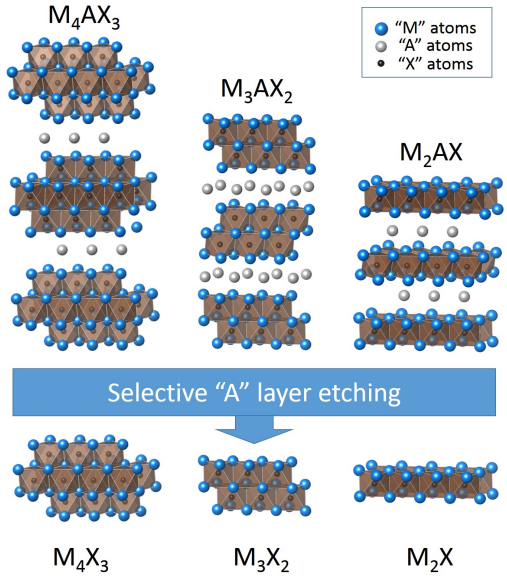

Figure 2.3 Synthesis process of MXenes by etching A atoms to separate into 2D MX layers [88] "From MAX to MXenes, structure" by Prussianblue1403 is licenced under CC BY-SA 3.0

Another interesting nanomaterial is molybdenum oxide which is classified as a transition metal oxide. Both fully oxidized (MoO_3) and substoichiometric (MoO_{3-x}) molybdenum oxide are studied for their abilities to emit heat from absorbing NIR light [89]. MoO_3 has an octahedral shape in an orthorhombic crystal structure [89]. MoO_3 has a large band gap and an insulating material. Only by removing oxygen from MoO_3, oxygen deficiencies are created which are found to affect the localized surface plasmon effect (LSPR) [89]. More details on the LSPR effect are discussed in section 2.4.1. Currently the best PTCE value for MoO_{3-x} nanoflakes is 37.53% [89]. There is potential to increase the PTCE value through changing the amount of oxygen deficiencies which can increase the absorbance in the NIR range. This is discussed in further detail in chapter 4.

Tungsten carbide (WC) is a metallic compound containing equal parts tungsten and carbon. The crystal structure of WC consists of a hexagonal lattice with a P-6m2 space group [84]. Tungsten carbide has not been thoroughly studied for photothermal therapy with only one study stating the PTCE value of 26% [91] in the NIR-I region. Tungsten semi-carbide (W_2C) is another form of WC and another 2D nanomaterial discussed in chapter 5 which is not well studied for photothermal therapy. W_2C displays metallic properties with a small or non-existent band gap which allow for a wide absorbance spectrum including in the NIR regions [84]. The crystal structure of W_2C is a hexagonal close packed (HCP) metallic lattice structure embedded with octahedral interstitials with alternating layers of carbon and tungsten arranged with a P-3m1 space group [84]. Currently W_2C has only had its photothermal properties studied in the NIR-II region which leaves photothermal properties in the NIR-I region unstudied. The PTCE value for W_2C in the NIR-II region is 46.8% [84] which shows promise for research in the NIR-I region.

Overall, many classes of 2D nanomaterials have been researched and are promising candidates for the future of nanomedicine. Table 2.1 shows a summary of the different PTCE values from various 2D nanomaterials.

Table 2.1 Photothermal conversion efficiencies of previously reported photothermal agents.

2D Nanomaterial	**Photothermal Conversion Efficiency (PTCE)**	**Reference**
Graphene	67%	[14]
Graphene Oxide	58%	[14]
Tungsten Disulfide with Bovine Serum Albumin (BSA)	13.2%	[16]
Tungsten Disulfide with Polyethylene Glycol (PEG)	35%	[17]
Tungsten Disulfide Quantum Dots	39.8%	[18]
Molybdenum Disulfide Nanosheets	24.37%	[19]
Molybdenum Disulfide Nanoflakes	27.6%	[20]
Molybdenum Disulfide in BSA and Folic Acid (FA)	54.2%	[21]
Titanium Carbide	30.6%	[25]
Niobium Carbide	37.6%	[26]
Tantalum Carbide	44.7%	[27]
Molybdenum Oxide (MoO_{3-z}) Nanoflakes	37.53%	[89]
Tungsten Semi-Carbide	46.8%	[84]

2.3 Advantages of Two Dimensional Nanomaterials

Selecting an ideal nanomaterial for photothermal therapy can be challenging as there are numerous factors to account for such as optical absorbance properties, surface area, particle size and synergistic potential with other cancer treatments. Two dimensional (2D) nanomaterials are considered promising photothermal agents due to unique optical absorbance properties, thin

structure and high surface area. Additionally, 2D nanomaterials have been shown to have potential with other cancer techniques such as photothermal therapy combined with chemotherapy.

Two dimensional (2D) nanomaterials are very diverse in properties, as talked about in the previous section, which prompts a variety of uses in biomedical applications such as medical imaging, drug delivery, biosensors and drug delivery [29]. The advantages of 2D nanomaterials are primarily in the large surface area ratios in comparison to nanomaterials of other dimensions which can allow for the functionalization of molecules such as drugs, fluorescent probes, proteins and even other nanoparticles [30].

Two dimensional nanomaterials are promising candidates for photothermal agents partially due to both the plasmonic properties and band-to-band excitation in the NIR region. For band-to-band excitation, quantum confinement causes an increase in the density of states at specific energy levels near the valence and conduction band. This increase in the density of states allows for a higher probability in exciting free electrons near the bandgap which leads to a higher light absorption in the NIR range [31]. Similarly, plasmonic nanomaterials absorb NIR light which causes electron oscillation which is converted to heat. Section 2.4 explains these phenomena in greater detail.

Since there are diverse groups of 2D nanomaterials, the electronic and optical properties will also vary, for example, TMDs will have varying optical properties depending on layer thickness. More specifically, bulk MoS_2 has an indirect bandgap while monolayer MoS_2 has a direct

bandgap resulting in monolayer MoS_2 absorbing photons with energy levels greater than the bandgap more easily than in bulk MoS_2 [32]. In a study by Zheng et. al, the absorbance properties of monolayer, few-layer and bulk MoS_2 were compared in which the optical absorbance of the monolayer MoS_2 was found to be higher than the few-layer and bulk MoS_2 [33].

Many studies have focused solely on the synthesis and optimization of 2D photothermal agents; however, due to the persistence of cancer cells, synergistic therapies which combine multiple treatment modalities are found to be more effective [34]. The research of 2D nanomaterials is still in the very early stages of development and there is still much to be done; however, with the advantages that 2D nanomaterials have over nanomaterials of other dimensions, 2D nanomaterials have a promising future in biomedical applications.

2.4 Photothermal Mechanisms

Most photothermal therapies involve using a near-infrared (NIR) laser in order to irradiate tumours either superficially or interstitially using an optical fibre laser probe which is inserted into the body to irradiate the tumour. Through the optical absorbance properties of nanoparticles at certain resonant wavelengths, the light energy from the laser can be converted into vibrational heat energy used to destroy or shrink tumours. The incoming light interacting with the nanoparticles causes vibration which generates heat. Choosing an ideal photothermal transducer can highly impact the optical absorbance properties of the nanoparticles within the tumour cells hence why wavelengths in the NIR ranges are chosen to best avoid interference from biological tissue. The NIR-I biological window is between 700-900 nm, while the NIR-II window is from 1000-1400 nm. Both of which allows for optimal optical absorbance of the nanoparticles

with minimal optical interference from biological tissues [6]. Either through antigen attachments to the tumour or through the enhanced permeability and retention effect, nanoparticles are brought into close proximity to the tumour to allow for direct irradiation of the tumour which will effectively generate enough heat to destroy the tumour.

For 2D nanomaterials, the photothermal mechanisms for converting NIR light into heat can be divided into two main groups. The first occurs primarily in metallic materials and is known as localized surface plasmon resonance (LSPR). The other mechanism occurs primarily in semiconducting materials and is known as non-radiative electron-hole pair generation and relaxation. Both types of mechanisms can contribute to the photothermal heating in 2D nanomaterials.

2.4.1 Localized Surface Plasmon Resonance

The most common occurrence of plasmonic resonance is in noble metal nanomaterials such as gold nanoparticles which have been the classic example for demonstrating the plasmonic effect. Gold nanoparticles have been observed to have a multitude of various colors due to the localized surface plasmon resonance (LSPR) effect. Similarly, 2D plasmonic nanomaterials have recently been studied and shown to have strong absorbance in the NIR range. MXenes and transition metal oxides (TMO) have strong plasmonic effects when irradiated by NIR light [35],[36]. The LSPR effect occurs on the metallic surface of the nanoparticle affecting the electrons on the surface of the metal. If the frequency of the incoming photon matches the natural resonance frequency of the electrons on the surface of the metal, then the electrons will oscillate accordingly. This results in the creation of a localized electric field which excites the electrons producing “hot electrons”. This produces heat via joule heating allowing the hot electrons to

dissipate the heat via electron-electron scattering which ultimately heats the nanomaterial and the surrounding area, as shown in Figure 2.4. More specifically, NIR light causes the oscillation of electrons which allows electrons to transfer from an occupied state to an unoccupied state which generates “hot electrons”. The “hot electrons” will then cool down by transferring thermal energy to the lattice phonons via scattering which results in increased temperature of the material [37]. Factors which affect the LSPR effect in 2D nanomaterials include the particles’ size and shape [38], the coulombic charge [39] and the dielectric constant. To reiterate, incoming light of a resonant frequency is used to excite a group of electrons such that they have a higher energy. As the electrons relax, the excess energy is converted into heat within the lattice resulting in an overall increase in temperature.

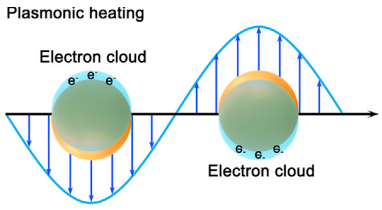

Figure 2.4 Plasmonic heating through the generation of “hot electrons” from the oscillating electric fields generated by absorbing light. Used with permission from Elsevier [43]

2.4.2 Electron-Hole Pair Generation and Relaxation

In semiconducting materials, photons with energy greater or equal to the semiconductors' band gap energy are absorbed. If the NIR light wavelengths irradiate the semiconducting material, an electron-hole pair is formed using the energy similar or greater than the bandgap of the semiconductor, as seen in Figure 2.5. As the electrons fall back down to lower energy states, the energy is given off as either radiating photons or non-radiative phonons depending on interactions with surface defects or dangling bonds [40]. Heat is then produced as the non-radiative phonons interact with the lattice creating a temperature increase proportional to the

light absorbed at the band gap energy. In narrow bandgap semiconductors, the energy of the incoming photons are usually greater than the bandgap energy which creates more electron-hole pairs [41]. Broad band gap semiconductors are more likely to re-emit the absorbed light as another photon via electron-hole recombination near the band edge, resulting in a poor photothermal performance [42]. This is similar to the photovoltaic process in which a semiconductors bandgap is used to convert light energy into electricity instead of heat.

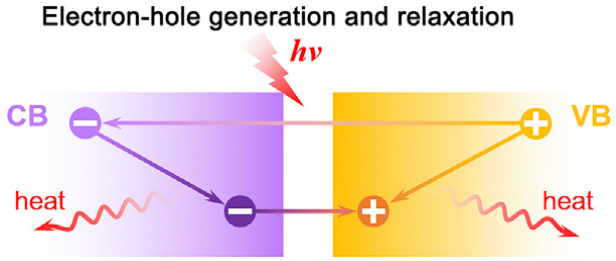

Figure 2.5 Electron-hole pairs are generated by photons with energies greater than the bandgap. Electrons from the valence band are excited into the conduction band past the band gap. As the electron and hole recombine, heat energy is given off as the electron and hole relax. Used with permission from Elsevier [43]

2.4.3 Thermal Vibrations of Carbonaceous Compounds

Nanomaterials containing carbon atoms such as graphene and graphene oxide are also able to absorb NIR light and convert the energy into heat through lattice vibrations. Carbon bonded atoms contain loosely held electrons that can be excited from the π (bonding) orbital to the π^*(anti-bonding) orbital with minimal energy from the irradiating light [43]. Electrons in the highest occupied molecular orbital (HOMO) are excited and promoted to the lowest unoccupied molecular orbital (LUMO) if the irradiating photon contains enough energy to cause the electron transition [44]. As the excited electron returns back down to the ground state, heat is released via lattice vibrations as demonstrated in Figure 2.6.

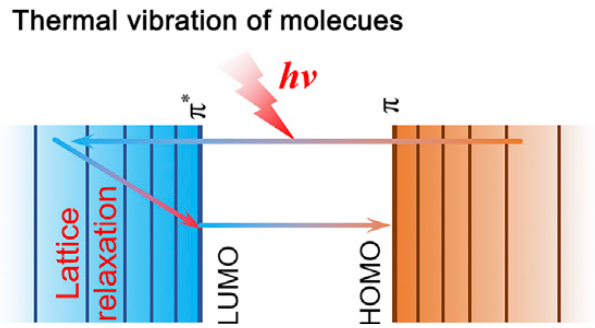

Figure 2.6 Electrons are excited and promoted from HOMO to the LUMO by an irradiating photon. Lattice vibrations as the electron relaxes generate heat. Used with permission from Elsevier [43]

2.5 Femtosecond Laser Applications in Nanomaterials

The femtosecond laser is a high-powered short-pulsed beam of light with the capability of influencing the properties of 2D nanomaterials. These properties include the size, shape, functional groups, optical properties and chemical structure. Ibrahim et al. were able to grow nanorods and nanotubes from 2D bulk flakes by using a femtosecond laser treatment process to control the aspect ratios of the rods [45]. The reduction of the 2D bulk flakes into smaller 2D nanorods and nanotubes is caused by Coulomb explosion which is caused by the high energy femtosecond laser. Coulomb explosion refers to the strong electric field generated at the focal point of the femtosecond laser, which is capable of breaking apart the bonds holding the bulk layer together [46]. In addition to controlling the shape and size of the nanomaterials, the femtosecond laser was also utilized to hybridize 2D nanomaterials by creating edge vacancies in MoS_2,WS_2 and BN flakes which were then functionalized with disassociated solvent molecules [46]. The versatility of the femtosecond laser creates unique opportunities to manipulate 2D nanomaterials with the possibility of enhancing and improving their photothermal conversion properties. In Chapters 4 and 5, MoO_{3-X} and W_2C materials formed using a femtosecond laser will be studied.

Chapter 3 Construction and Testing of a Photothermal Conversion Efficiency Measurement System

3.1 Measuring the Photothermal Conversion Efficiency

The primary method of determining the photothermal conversion efficiency in nanomaterials is to use the time constant method which measures the change in heat occurring within a cuvette containing a solution of the nanomaterial compared with the surroundings. This is usually done using a thermocouple which measures the temperatures inside and outside the cuvette at a given time. The light source is usually a low powered continuous wave NIR laser. Figure 3.1 shows a simple configuration of an experimental setup involved in measuring the PTCE.

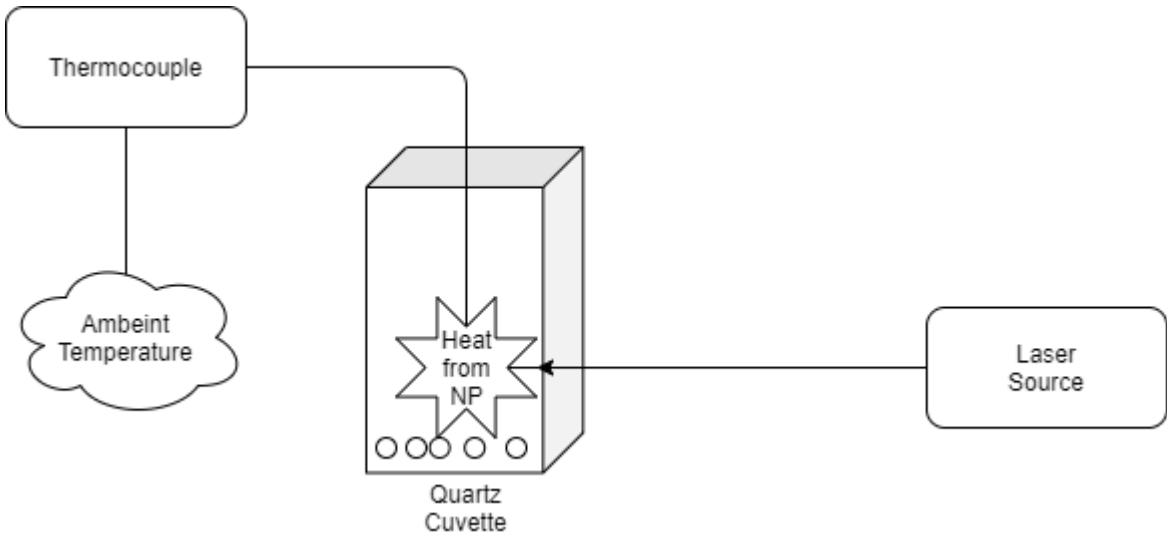

Figure 3.1 Experimental setup to measure the photothermal conversion efficiency. Thermocouples are used to measure both the nanoparticle solution temperature and the ambient temperature.

To start, the nanoparticle solution temperature must be equivalent to the ambient temperature to minimize contact heating when transferring the nanoparticle solution between containers. Once the temperatures have equalized, the irradiating source is turned on and the nanoparticle solution temperature is recorded. During this time, the nanoparticle solution temperature should increase and plateau, reaching a maximum temperature at which the irradiating laser is turned off, allowing the nanoparticle solution to cool back to the ambient temperature. A typical heating and

cooling plot of the changes in temperature can be seen in Figure 3.2. It shows the heating and cooling of a nanoparticle solution containing tungsten carbide powder dissolved in 1 mL of acetonitrile, which was formed by irradiating 0.125 mg of WS_2 with a 0.39 watts continuous wave laser with a wavelength of 808 nm, as discussed in Chapter 5.

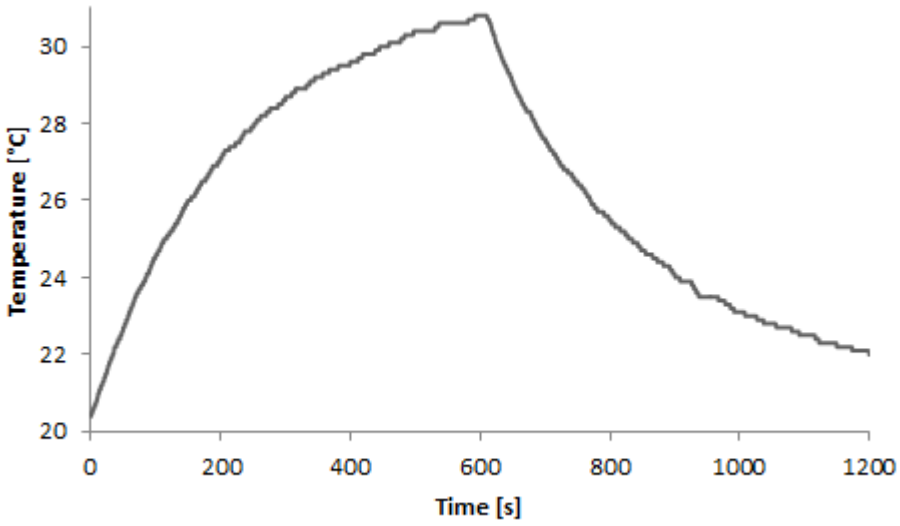

Figure 3.2 Temperature change over time for tungsten carbide dissolved in acetonitrile. Laser turned on for 600 seconds corresponding to the heating phase. Similarly, the laser is turned off for 600 seconds to observe the cooling phase.

Based on the temperature curve shown in Figure 3.2, an equation for solving the photothermal conversion efficiency can be derived. Originally Roper et al.used these equations to describe the photothermal conversion efficiency of plasmonic gold nanoparticles [48]. However this equation can be applied to any nanomaterials which exhibit photothermal heating via laser irradiation. From the law of conservation of energy, an energy balance equation can be used to explain the energy transfer relationship in Figure 3.1. The energy balance of this system can be described by Equation (1).

$$\sum_{n=i} m_i C_{p,i} \frac{dT}{dt} = Q_I + Q_0 - Q_{ext} \qquad (1)$$

Where the terms $m_iC_{p,i}$ refer to the mass and heat capacity of each of the system components which include the nanoparticles, solvent and container. The aggregate system temperature is represented as T and t is the system time. The right hand side of the equation includes a sum of all the energy terms in the system which includes Q_I which is the heat dissipated by the electron-phonon relaxation, Q_0 which is the heat dissipated by the quartz cuvette container and Q_{ext} which is the external heat flux of the system.

The electron-phonon relaxation of a nanoparticle solution induced as a result of irradiation with a laser at the resonant wavelength λ can be described by Equation (2).

$$Q_I = I(1 - 10^{-A_\lambda})\eta \qquad (2)$$

The power of the irradiating laser is described by I and the efficiency of transducing the resonant absorbance energy to thermal energy, also known as the photothermal conversion efficiency, is described by η. The absorbance of the nanoparticle solution at the wavelength λ of the irradiating laser is A_λ.

The rate of heat transfer between the solution and the container is defined as Q_{ext} and is proportional to the linear thermal driving force multiplied by the heat transfer coefficient which is described in Equation (3).

$$Q_{ext} = hA(T(t) - T_{amb}) \qquad (3)$$

Where h is the system heat transfer coefficient, A is the surface area of the container where the heat transfer occurs, T_{amb} is the ambient temperature at the beginning of the experiment and $T(t)$ is the temperature measured with respect to time t.

To solve for hA which is difficult to measure, a dimensionless driving force temperature is introduced which is θ. The equation for the driving force temperature is shown in Equation (4).

$$\theta = \frac{T_{amb} - T(t)}{T_{amb} - T_{max}} \qquad (4)$$

Where T_{max} is the maximum temperature reached during laser irradiation which occurs just before the cooling phase of the experiment when the laser is turned off.

The system time constant τ_s is introduced which relates the system heat transfer coefficient h and the surface area of heat transfer A with the mass m_i and heat capacity C_i of the system. The mass and heat capacity of the system is usually approximated using the solvents mass and heat capacities because the amount of nanoparticles in comparison to the solvent is usually small.

Therefore the mass and heat capacity of the nanoparticles is insignificant and typically ignored. Equation (5) explains the relation aforementioned.

$$\tau_s = \frac{\sum_i m_i C_{p,i}}{hA} \qquad (5)$$

From Equation (4), a relation between the rate of change in temperature over time and the rate of change in the driving force temperature is found by taking the derivative of Equation (4) to create Equation (6).

$$\frac{dT}{dt} = \frac{d\theta}{dt}(T_{max} - T_{amb}) \qquad (6)$$

Substituting Equations (3),(4),(5) and (6) into Equation (1) results in Equation (7) after a series of rearrangements.

$$\frac{d\theta}{dt} = \frac{1}{\tau_s}\left[\frac{Q_I - Q_0}{hA(T_{max} - T_{amb})} - \theta\right] \qquad (7)$$

During the cooling phase just after the irradiating laser is turned off, $Q_I + Q_0 = 0$ indicating that the system is cooling in which no heat is being generated. This simplifies Equation (7) into Equation (8).

$$\frac{d\theta}{dt} = \frac{-\theta}{\tau_s} \qquad (8)$$

Taking the integral of both sides of Equation (8) and solving using the initial conditions of $\theta = 1$ and $t = 0$, a relation between the system time and the driving force temperature can be solved, resulting in Equation (9).

$$\theta = e^{\frac{-t}{\tau_s}} \qquad (9)$$

By taking the natural logarithm of both sides, the Equation (9) can be further simplified to Equation (10) which allows the system time constant τ_s to be the slope of the linear equation.

$$\tau_s = \frac{-t}{ln(\theta)} \qquad (10)$$

Similarly, while under laser irradiation, $Q_I + Q_0$ is finite as the temperature increases to a maximum. This can be described in Equation (11) which occurs when the external heat flux Q_{ext} given by Equation (3) is equal to the heat input provided by the laser irradiation Q_I.

$$Q_I + Q_0 = hA(T_{max} - T_{amb}) \qquad (11)$$

Substituting Equation (11) into Equation (7) simplifies to Equation (12).

$$\frac{d\theta}{dt} = \frac{1}{\tau_s}(1-\theta) \qquad (12)$$

When taking the integral of both sides of Equation (12) and using the initial conditions of $\theta = 0$ and $t = 0$, a similar relation between the driving force temperature θ and system time τ_s can be solved as seen in Equation (13).

$$\theta = 1 - e^{\frac{-t}{\tau_s}} \qquad (13)$$

Again, a linear relation can be obtained from Equation (13) by taking the natural logarithm of both sides resulting in Equation (14).

$$\tau_s = \frac{-t}{ln(1-\theta)} \qquad (14)$$

Therefore, by using the linear driving force approximation, a line of best fit can be obtained from the time versus temperature curves to accurately represent the system time constant τ_s. This is demonstrated in Figure 3.3 using the cooling phase temperature data from the same tungsten carbide sample dissolved in acetonitrile shown in Figure 3.2. Then, the measured system time constant τ_s can be inserted into Equation (5) and rearranged to solve for both the unknown heat transfer coefficient h and the surface area of heat transfer A.

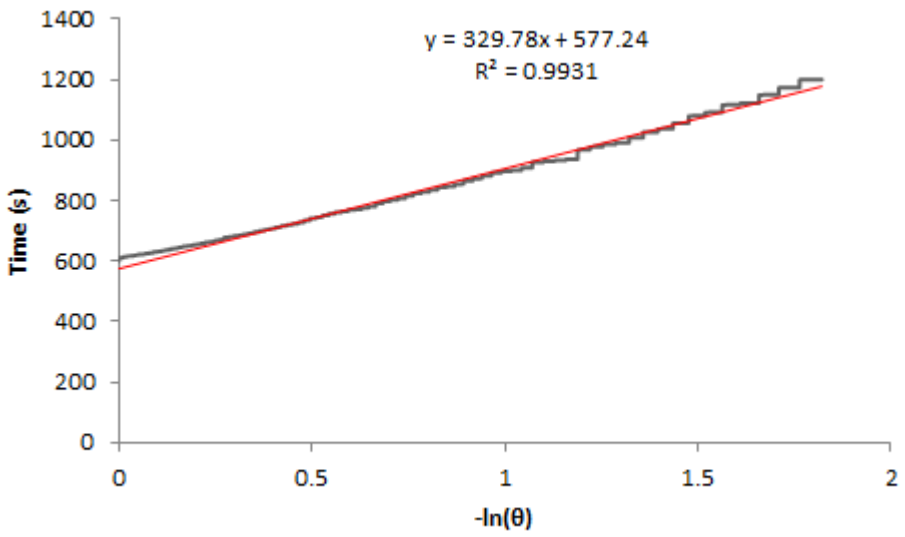

Figure 3.3 Approximation for the time constant via the slope. Line of best fit shown by red line. Time constant is 329.78 seconds.

It is important to note that Equation (10) and Equation (14) are analogous and can both be used to determine the system time constant τ_s. Using Equation (10) determines the system time constant τ_s using temperature data after the laser is turned off (also known as the cooling phase) and Equation (14) used the temperature data while the nanoparticle sample is in the heating phase.

Finally, the equation to measure the photothermal conversion efficiency η can be obtained by substituting Equation (2) into Equation (11) to create Equation (15).

$$\eta = \frac{hA(T_{max} - T_{amb} - Q_0}{I(1 - 10^{-A_\lambda})} \qquad \mathbf{(15)}$$

Where Q_0 represents the heat dissipated by the system excluding the nanoparticles. This is measured similarly to the aforementioned heating and cooling time constant method; however,

the experiment is conducted with the solvent only as opposed to the nanoparticle solution. Therefore a similar equation representing Q_0 can be solved as seen in Equation (16).

$$Q_0 = h_{solvent} A_{solvent} (T_{max,solvent} - T_{amb,solvent}) \qquad \mathbf{(16)}$$

Solving for the heat transfer coefficient for the solvent $h_{solvent}$ and the surface area of heat transfer for the solvent $A_{solvent}$ is similar to solving for the heat transfer coefficient h and surface area of heat transfer A in Equation (5) with the exception of using the laser to irradiate the solvent only without any nanoparticles.

In conclusion, the photothermal conversion efficiency of any nanomaterials can be determined by irradiating the nanoparticle solution with a continuous NIR laser and recording the temperature changes over time. Once the maximum temperature of the nanoparticle solution is reached, the laser is turned off allowing the nanoparticle solution to cool back down to ambient temperature. Using the recorded temperature change data, a system time constant can be obtained by fitting either the heating or cooling phase. The system time constant is then used to solve for the unknown heat transfer coefficients and the total surface area of the solution. This is then repeated again to solve for the heat generated without the nanoparticles by measuring only the temperature change of the solvent. Finally with the known parameters, the photothermal conversion efficiency can be determined.

3.2 Design of a Photothermal Conversion Efficiency System

The design of the photothermal conversion efficiency system (PTCE) starts with selecting good components which can accurately measure the parameters mentioned in section 3.1. The equation for the photothermal conversion efficiency contains three key parameters which must be measured. These parameters are the temperature, laser power and the absorbance of the nanoparticle solution at the irradiating wavelength. To ensure optimal irradiation of the nanomaterials, an appropriate NIR continuous wave laser must be chosen based on previously reported research.

To measure the temperature, either a direct contact or non-contact approach could be taken. More specifically, using a thermocouple probe to measure the nanoparticle solution would be considered direct contact. Likewise, using an infrared camera to measure the temperature would be a non-contact approach as the nanoparticle solution would not be touched. Intuitively, using a non-contact approach would be ideal due to the fact that the risk of contaminating the nanoparticle solution is minimal as compared to a direct contact approach. However this can be easily remedied by using proper cleaning techniques to ensure no cross contamination occurs between testing multiple samples. On the other hand, the advantage of using a thermocouple contact probe as opposed to a non-contact infrared thermometer would be the ability to measure the body of the nanoparticle solution as opposed to just the surface. This may pose an issue as uneven heating could provide an inaccurate temperature reading at the surface. However this can also be remedied by using a magnetic stir bar to mix the nanoparticle solution to have a uniform temperature. The main advantage of using the direct contact thermocouple probe is the accuracy of the temperature data in comparison to using an infrared non-contact method. Multiple studies

have shown that there is poor agreement in measured temperature between the infrared devices and the contact devices [49]. During heating, infrared devices were found to be unsuitable for monitoring the temperatures as opposed to the conductive contact method [50]. Therefore a direct contact thermometer as shown in Figure 3.4 was chosen to accurately measure and log the temperature changes of the nanoparticle solution as it is irradiated by a NIR laser. The thermometer is capable of measuring two different temperatures using a type K thermocouple probe. A resistance thermometer detector was also considered as they are generally more accurate versus thermocouples however due to the expensive costs, a thermocouple was ultimately selected.

Figure 3.4 Fisherbrand thermocouple reader used to measure solution and ambient temperatures simultaneously.

To record the temperature data, a custom program written by co-op student Cindy Yu in LabView was created. The user interface is shown in Figure 3.5. The program allows a direct serial connection to the thermocouple probe which can show the temperature changes in real time. Both the nanoparticle solution temperature and the ambient temperature can be simultaneously measured and recorded due to the dual probe functionality of the thermocouple reader. The data is then written to an excel file in which it can then be further processed in order to calculate the PTCE.

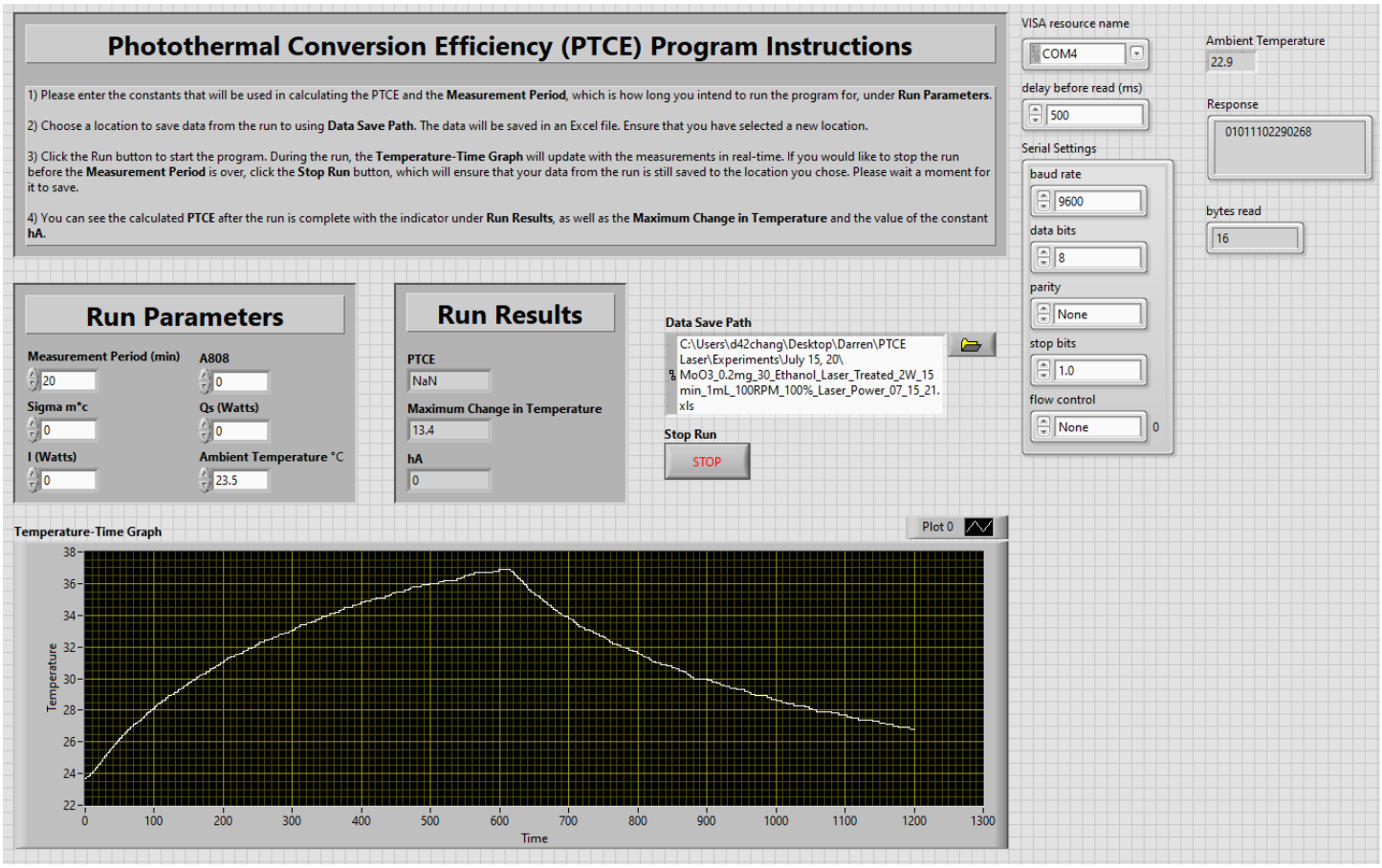

Figure 3.5 Graphical user interface for the LabView program that records temperature data from the thermocouple reader and exports it to an excel file for further processing.

In order to measure the NIR laser power, an appropriate laser power meter must be chosen. Currently there are two main types of laser power meters, calorimeter and pyroelectric. The calorimeter laser power meter measures laser power over time, meaning that power measurements will be averaged over time [51]. The response time of calorimeter laser power meters are usually much slower than pyroelectric laser power measurements. On the other hand, pyroelectric laser power meters are relatively quick in response and measure the change in energy of the laser power [51]. Therefore a pyroelectric laser power meter shown in Figure 3.6 was chosen to measure the power of the continuous wave NIR laser.

Figure 3.6 Gentec-EO laser power meter used to determine the power of the NIR laser.

To measure the absorbance of the nanoparticle solution an absorbance spectrometer can be used to determine the absorbance value at the irradiating wavelength. A blank solution containing only the solvent is used as the reference and is compared against the solution containing the nanoparticles. The logarithmic difference in the transmittance of both the solvent and the nanoparticle solution is measured and used to calculate the absorbance curves. More details are explained in Chapter 3.3.

From literature, the NIR-I range corresponds to 700-900 nm wavelengths while the NIR-II window is from 1000-1400 nm which allows for the optimal absorbance of the nanoparticles with minimal interference from biological tissues [6]. Therefore a 808 nm continuous wave laser was chosen to irradiate nanomaterials in the NIR-I range as this is a common wavelength used in photothermal research. An appropriate collimating lens was specifically chosen for the laser to convert the naturally divergent beam of the NIR lasers to a collimated beam. More specifically the collimated beam is reduced to a spot size of ~5 mm to accommodate the quartz cuvette having a path length of 10 mm and a width of 10 mm. This allowed for the entire laser beam to

pass through the quartz cuvette with minimal reflectance or divergence.The average laser power of the 808 nm laser was ~0.375 watts (W) which corresponds to a laser power density of ~1.91 W/cm^2.

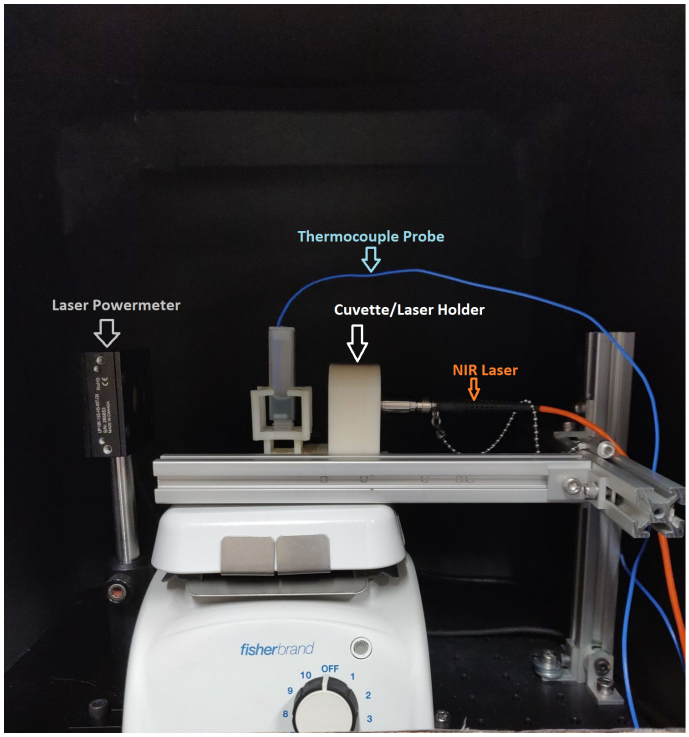

Figure 3.7 PTCE measurement setup. The NIR laser is the orange cable. Thermocouple probe in blue. A Fisherbrand magnetic stirrer used to maintain uniform solution temperatures. Gentec-EO laser power meter shown in black on the left. Cuvette holder in white aligns the NIR laser to the center of the cuvette.

Putting all the components together, a photothermal conversion efficiency measurement system is created as seen in Figure 3.7. A custom 3D printed part (created by co-op student Cindy Yu) was designed to secure the NIR-I irradiating laser while also holding the quartz cuvette containing the nanoparticle solution as seen in Figure 3.8. More specifically, the 3D printed part holder allows for the laser to align directly and irradiate through the center of the quartz cuvette containing 1 mL of nanoparticle solution. This allows the laser beam to pass directly through the quartz cuvette, irradiating the nanoparticle solution efficiently. Also, the 3D printed part holder is designed to allow minimal contact between the holder and the quartz cuvette to minimize heat

exchange with the holder. The plastic cuvette lid had a hole drilled in the corner to allow the thermocouple probe (in blue) to contact the nanoparticle solution to record the temperatures. The corner of the cuvette lid was chosen to allow the thermocouple probe to rest near the corner of the cuvette to prevent the laser beam directly passing through the probe tip causing inaccurate temperature increases. The secondary thermocouple probe is placed outside the system in order to measure the ambient temperature. A magnetic stirrer is also placed under the quartz cuvette with a magnetic stir bar placed in the nanoparticle solution in order to maintain a uniform temperature within the nanoparticle solution. The laser power meter is strategically placed in range of the laser beam path such that if the quartz cuvette were to be removed, there would be a clear path from the laser to the power meter. This allows for the laser power to be measured at the start of each experiment without having to align the laser beam path. It is important to note that the apparatus can also be adjusted in all 3 axes to accommodate for any misalignment with the magnetic stirrer or the laser power meter. For safety, the whole system is enclosed to prevent any stray laser beams from hitting an unwanted target. The 3D CAD model shown in Figure 3.8 was designed for minimal contact such that the heat transfer between cuvette and the holder is negligable.

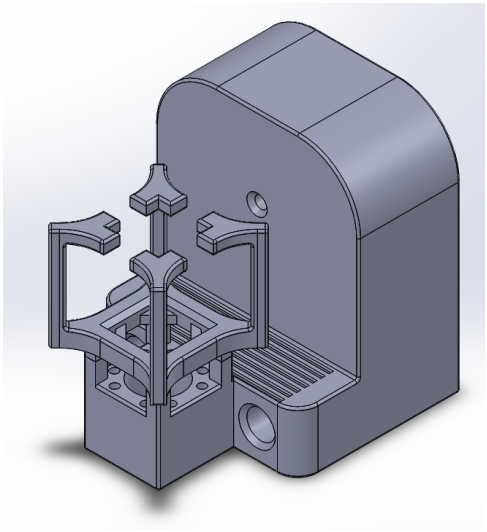

Figure 3.8 3D CAD model of cuvette/laser holder created in Solidworks

Overall, a robust system is designed to allow for the measurement of the required parameters for calculating the photothermal conversion efficiency of any nanoparticle solution. The temperature is measured via a direct contact thermocouple probe which is able to simultaneously measure both the nanoparticle solution and the ambient temperature. A custom program written in LabView was used to interface with the thermocouple reader in order to export the temperature data to an excel file for further processing. A pyroelectric laser power meter is chosen to measure the instantaneous laser power. An 808 nm continuous wave laser was chosen to represent laser irradiation from the NIR-I biological window. Along with absorption measurements from external equipment described in section 3.3, the photothermal conversion efficiency of any nanoparticle solution can be measured and calculated.

3.3 Preparation of Photothermal Agents

The starting nanomaterials used in this work are tungsten disulfide (WS_2), molybdenum disulfide (MoS_2), titanium aluminum carbide (Ti_3AlC_2) and tungsten carbide (WC). Both WS_2 and MoS_2 were irradiated with the femtosecond laser by PhD student Fan Ye. Specific details for MoS_2 and WS_2 are found in chapters 4 and 5 respectively. The femtosecond laser used was a Spitfire Ace-35F with a 800 nm wavelength, 35 femtosecond pulse duration and a 1 kHz refresh rate. Figure 3.9 shows the femtosecond laser configuration which includes a convex lens that focuses the laser beam in the center of the nanoparticle solution. The magnetic stir bar is used to maintain a uniform nanoparticle solution to ensure uniform femtosecond laser irradiation. Calibration of the femtosecond laser system was also preformed by Fan Ye.

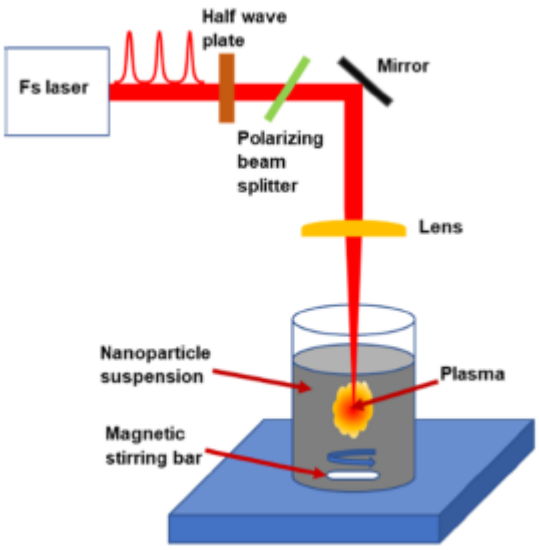

Figure 3.9 Configuration of the femtosecond laser irradiating a nanoparticle suspension.

The WS_2 bulk powder was purchased from Graphene Supermarket with a purity of 99%. The average particle size of the WS_2 powders is ~90 nm in diameter. The WS_2 bulk powder was dissolved into acetonitrile creating a 0.25 mg/mL concentrated solution. Similarly, MoS_2 bulk powder was also purchased from Graphene Supermarket with a purity of 99%. The average particle size is ~90 nm in diameter. The MoS_2 bulk powder is dissolved into ethanol-water solutions with a concentration of 0.125 mg/mL. Both the WS_2 and MoS_2 solutions were first sonicated for at least 10 minutes to disperse the powders into the solvents before being subjected to femtosecond irradiation experiments as discussed later in chapters 4 and 5 respectively. It is important to note that the femtosecond laser is used to partially oxidize the MoS_2 solution. The MoS_2 bulk powder is first dissolved into 80% ethanol/water through ultrasonication with a concentration of 0.125 mg/mL and is then subjected to 2 W of femtosecond irradiation for 30 minutes. The result is a plasmonic substoichiometric molybdenum oxide which is later used to test the photothermal stability as discussed later in section 3.5.1.

In addition, MoS_2 monolayer powder purchased from Ossila with a purity of >99% was dissolved in pure water with a concentration of 0.125 mg/mL. The flake size of the MoS_2 powders is between 0.1-0.4 μm with a flake thickness between 0.6-1.2 nm. The MoS_2 monolayer solution was sonicated for at least 10 minutes or until the solution was visually uniform. Similarly, WS_2 monolayer powder was also purchased from Ossila with a purity of >99% and was dissolved in pure water with a concentration of 0.125 mg/mL. Similarly the flake size of the WS_2 powders is between 0.1-0.4 μm with a flake thickness between 0.6-1.2 nm. Both the MoS_2 and WS_2 monolayer powder solution were used to test the repeatability of the PTCE setup as shown in section 3.5.1.

Ti_3AlC_2 powder was prepared by PhD student Fan Ye and was purchased from Shanghai Xinglu with a purity of 99% and a chemical composition of 73.8% titanium, 13.76% aluminum and 12.24% carbon. The particle size was <74 μm and was etched in a solution of pure HCl to remove the aluminum layer. Then the solution was centrifuged at 5000 RPM and washed with pure water. After washing and centrifuging five times, the supernatant was taken as the final solution. The resultant titanium carbide was then used in section 3.5.2 to measure the PTCE as the NIR laser power is varied.

The WC powder was purchased from Sigma Aldridge with a purity of >99% and was dissolved in both pure water and acetonitrile. Both solutions had a concentration of 0.125 mg/mL and were sonicated for a minimum of 10 minutes. The WC solutions are used to confirm the consistency of the PTCE measurements of the same nanoparticle dissolved in different solvents as described in section 3.5.3.

3.4 Comparison of Absorbance Measurements for Photothermal Conversion Efficiency Calculations

The majority of the absorbance measurements were acquired using a spectrofluorometer. Typically absorbance spectra are measured automatically using a UV-Vis spectrophotometer, however access to this equipment was limited and the readily available spectrofluorometer was capable of performing these measurements. The number of photons that pass through the sample determines the transmittance of the material. By taking the negative natural logarithm of the transmittance, as shown in Equation (17), the absorbance of the material can be measured.

$$A = -log_{10}(T) \qquad \mathbf{(17)}$$

As the nanoparticle absorbance is an important parameter for determining the PTCE, measurements performed using different instruments and cuvettes were compared to ensure accuracy. The blue curves in Figure 3.10 are measurements performed using a Shimadzu UV-2501PC spectrophotometer and a plastic cuvette, the red curves are measurements performed using a Molecular Devices SpectraMax M5 UV-Vis spectrophotometer using a quartz cuvette, and the green curves are measurements done using the Horiba Quantamaster 8000 spectrofluorometer using a quartz cuvette. Figure 3.10a shows absorbance curves of monolayer tungsten disulfide, Figure 3.10b shows the absorbance curves for monolayer molybdenum disulfide, Figure 3.10c shows the absorbance curves for bulk tungsten disulfide, and Figure 3.9d shows the absorbance curves for bulk molybdenum disulfide. The monolayer WS_2 and MoS_2 were purchased from Ossila while the bulk WS_2 and MoS_2 were purchased from Graphene

Supermarket. Each WS_2 and MoS_2 powdered sample was dissolved in pure water using an ultrasonicator.

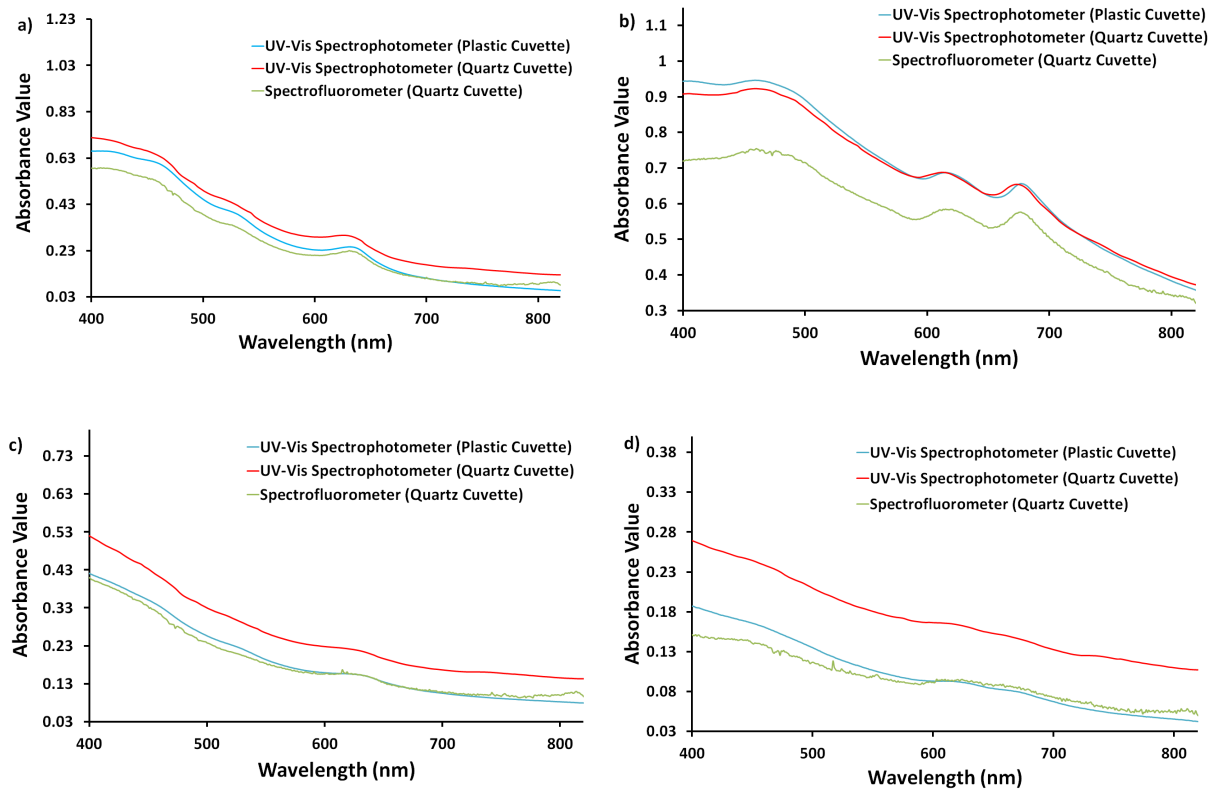

Figure 3.10 UV-visible absorbance spectra of (a) monolayer tungsten disulfide. (b) monolayer molybdenum disulfide (c) multilayer tungsten disulfide (d) multilayer molybdenum disulfide. UV-Vis spectrophotometer absorbance spectra measurement is performed with a plastic cuvette in blue. UV-Vis spectrophotometer absorbance spectra measurement is performed with a quartz cuvette in red. Absorbance spectra measurement is performed with a spectrofluorometer in a quartz cuvette in green.

The bulk MoS_2 and WS_2 show relatively flat absorbance curves, while the monolayer MoS_2 and WS_2 show prominent peaks indicating monolayers. For monolayer MoS_2 the two sharp peaks at ~615 nm and ~675 nm correspond to the absorption owing to the direct transitions at the K point of the Brillouin zone which corresponds to the generation of B and A excitons respectively [52],[53]. Similarly for monolayer WS_2, excitonic absorption peaks at ~530 nm and ~630 nm also appear due to the direct band gap transitions from the K point of the Brillouin zone which correspond to the B and A excitons respectively [54].

From figures 3.10 a-d, the absorbance curves from each source shows that all peaks and features are captured accurately. Therefore, absorbance measurements obtained with the spectrofluorometer can be considered accurate enough for PTCE measurements. Deviations in the magnitude of the absorbance spectra can be attributed to some samples containing less volume than required for UV-vis measurements. It is also important to note that absorbance measurements taken this way are approximations based on the transmittance of the material. More specifically not all of the light that is not transmitted is necessarily absorbed, as some light may be reflected or scattered from the cuvette.

3.5 Testing of the Photothermal Conversion Efficiency System

In order to confirm the accuracy, repeatability and reliability of the photothermal conversion efficiency system, three main experiments are conducted. The first includes repeating the same PTCE measurements for the same nanomaterials on different dates. The second experiment repeats the PTCE measurements with different NIR laser powers. The third experiment involves measuring the PTCE of the same nanomaterial dissolved in different solvents. Ideally in each of the three experiments, the measured PTCE values should be very similar as the PTCE is dependent only on the nanomaterial.

3.5.1 Repeatable Measurements

MoS_2 monolayer powder purchased from Ossila with a purity of >99% was dissolved in pure water with a concentration of 0.125 mg/mL and measured multiple times on different dates, as shown in Table 3.1. As expected, performing multiple PTCE measurements on the same material at different times resulted in very similar PTCE, absorbance, temperature change values and time

constants. Variations in the PTCE values can be attributed to experimental uncertainty, systematic errors and random errors, such as inaccuracies when measuring the volume of samples due to poorly calibrated equipment or random room temperature fluctuations during measurement.

Table 3.1 Repeated PTCE measurements of monolayer molybdenum disulfide dissolved in water.

Day of Measurement	**PTCE**	**Absorbance at 808 nm**	**Temperature Change (°C)**	**Time Constant τ_s**
Day 1	14%	0.224	3.9°C	557s
Day 5	12%	0.245	4.1°C	516s
Day 6	14%	0.234	3.8°C	518s
Day 11	15%	0.199	3.9°C	573s

Furthermore, to test the reliability of the temperature measurements, cyclic heating and cooling via irradiation and no irradiation was measured, as seen in Figure 3.11. Femtosecond laser-treated MoS_2 dissolved in an 80% ethanol/water solution as prepared in section 3.3 was used to measure cyclic heating and cooling. Results show that in the five cycles of heating and cooling, the MoS_2 was photothermally stable demonstrating the repeatability of the measurement technique.

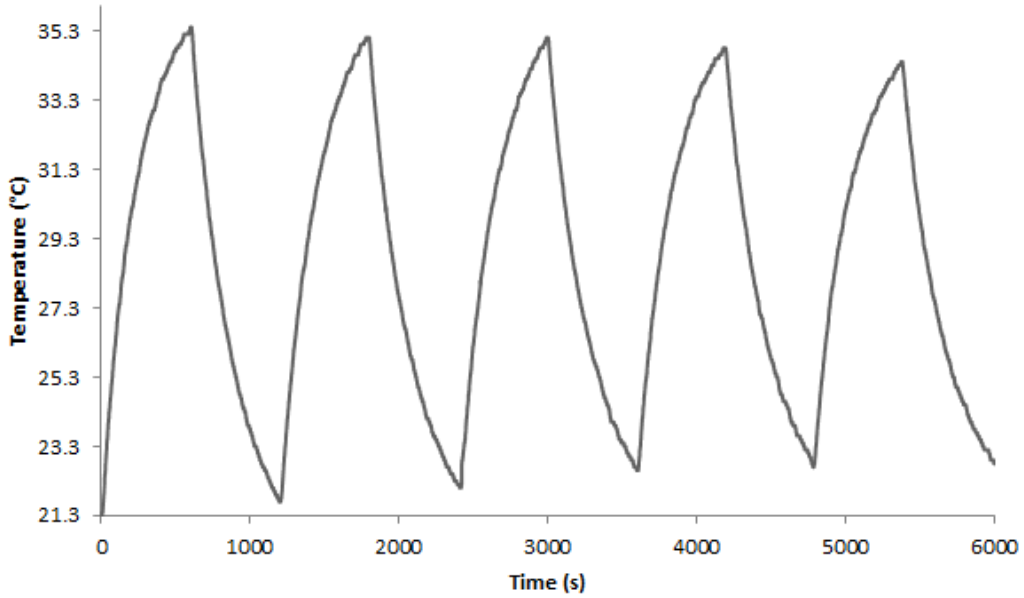

Figure 3.11 NIR laser is turned on and off every 600 seconds to create a cyclic heating and cooling curve. Femtosecond laser irradiated MoS_2 is photothermally stable.

3.5.2 Varying Laser Power

A similar experiment was conducted on chemically etched titanium aluminum carbide dissolved in water where multiple PTCE measurements were taken, however the laser power for the PTCE measurement was changed to 25%, 50%, 75% and 100% maximum power. The results shown in Table 3.2 also are expected as the PTCE should be independent of the laser power. However with decreasing laser power, the temperature changes also decrease proportionally as expected. In literature, 2D titanium carbide nano sheets were found to have a PTCE of around 34% [55],[56],[57], which is quite comparable to the results shown in Table 3.2. Discrepancies in the PTCE values found in literature can be attributed to different synthesis methods, doping of other nanomaterials and different concentrations used.

Table 3.2 PTCE measurement values performed with varying NIR laser powers (0.48, 0.35, 0.24 and 0.072W).

Laser Power 3.5.3 Varying Solvents	**PTCE**	**Absorbance at 808 nm**	**Temperature Change (°C)**	**Time Constant τ_s**
100% Laser Power 0.48W	37%	0.398	12.2°C	476s
75% Laser Power 0.35W	36%	0.377	8.8°C	487s
50% Laser Power 0.24W	38%	0.365	6.1°C	481s
25% Laser Power 0.072W	38%	0.394	2.1°C	507s

The final experiment was conducted with tungsten carbide nanopowder dissolved in two different solvents. Water and acetonitrile were chosen as they are vastly different solvents with different properties. The main difference is that water is a polar protic solvent while acetonitrile is a polar aprotic solvent. In addition, water contains both hydrogen and oxygen however acetonitrile consists of carbon, hydrogen and nitrogen. Results are shown in Table 3.3. The same PTCE was obtained for both solvents, showing that the nanoparticles are strictly responsible for the measured PTCE. However, this is not the case if the nanoparticle solution is treated by the femtosecond laser, in which case the solvent plays a crucial role in changing the nanomaterial, inherently changing the PTCE values. This phenomena will be discussed more in Chapters 4 and 5. In the literature, tungsten carbide is found to have a PTCE value of 26% [58] which is comparable to PTCE values found experimentally.

Table 3.3 PTCE measurement values of tungsten carbide dissolved in both water and acetonitrile. PTCE values are independent of the solvent.

Solvent	**PTCE**	**Absorbance at 808 nm**	**Temperature Change (°C)**	**Time Constant τ_s**
Water	20%	0.361	6.2°C	547s
Acetonitrile	20%	0.424	9.1°C	324s

Overall, this series of experiments have shown that the general design of the photothermal conversion efficiency system is accurate and reliable. Similar PTCE values are obtained when the same material is measured on different occasions, the PTCE is independent of the laser power and solvent, and the experimentally measured PTCE values are similar to those reported in literature.

Chapter 4 Photothermal Agent: Molybdenum Oxide

4.1 Synthesis of Plasmonic Substoichiometric Molybdenum Oxide via Femtosecond Laser Treatment

The synthesis of plasmonic substoichiometric molybdenum oxide was performed by PhD student Fan Ye. The femtosecond laser was used to partially oxidize molybdenum disulfide. More specifically, MoS_2 powders were dissolved into ethanol/water mixtures and irradiated by a femtosecond laser which caused Coulomb explosion, exfoliation and oxidation. The femtosecond laser exfoliates the layers of MoS_2 by breaking the van der Waals forces holding the 2D layers together. Meanwhile, either water or ethanol will create reactive oxygen species such as O^+ and O^{2+} which will interact with the MoS_2 sheets to help partially oxidize the MoS_2. Newly formed $-OH_2$ groups will react with MoS_2 and create Mo-OH_2 bonds as the reactive oxygen species continues to oxidize the MoS_2. Finally as the $-OH_2$ groups are released from the lattice, H_2O and plasmonic molybdenum oxide (MoO_{3-x}) are formed. By further laser treating the MoO_{3-x}, full oxidation occurs, creating MoO_3. The morphology of the material also changes from MoO_{3-x} nanosheets to MoO_3 nanobelts. A summary of the synthesis process can be viewed in Figure 4.1 [47]. It is important to note that Fan Ye's work in identifying the formation mechanism of the plasmonic MoO_{3-x} is crucial to understanding the photothermal conversion efficiency. All of the synthesis and material characterization was done by Fan Ye and is detailed in Reference [47]. Although not shown in this work, SEM and AFM images are shown in Reference [47] demonstrating the micro-structures formed using the femtosecond laser.

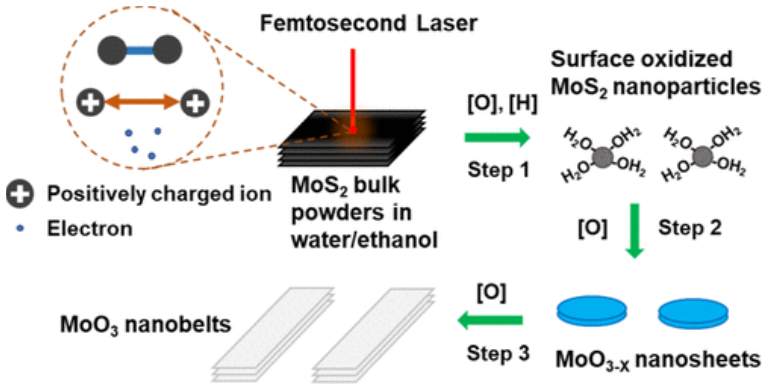

Figure 4.1 Synthesis overview of MoO_{3-x}. A femtosecond laser is used to separate the bulk layers of MoS_2. Partial oxidation of MoS_2 is the result of femtosecond laser irradiation with an ethanol/water mixture. Longer femtosecond irradiation times change the shape and fully oxidize the MoO_{3-x} nanosheets to MoO_3 nanobelts.

Raman spectra provided by Fan Ye shows the partial oxidation of MoS_2 in 80% ethanol/water in Figure 4.2. E_{2g} and A_{1g} peaks are observed in the original MoS_2 powder before any femtosecond laser treatment; however, as the MoS_2 samples are femtosecond laser treated, the E_{2g} and A_{1g} peaks start to disappear as new peaks (dashed red lines) corresponding to MoO_{3-x} start to appear at 195, 222, 350, 489 and 725 cm^{-1}. The MoO_{3-x} peaks were especially prevalent for the sample that was treated at 2W for 30 minutes, as opposed to laser treating the MoS_2 sample at 2W for 10 minutes or 50 minutes. The orange arrows in Figure 4.2 correspond to the formation of hydrogen-bonded molybdenum oxide (H_xMoO_3), which is formed early around 10 minutes into the femtosecond laser treatment.

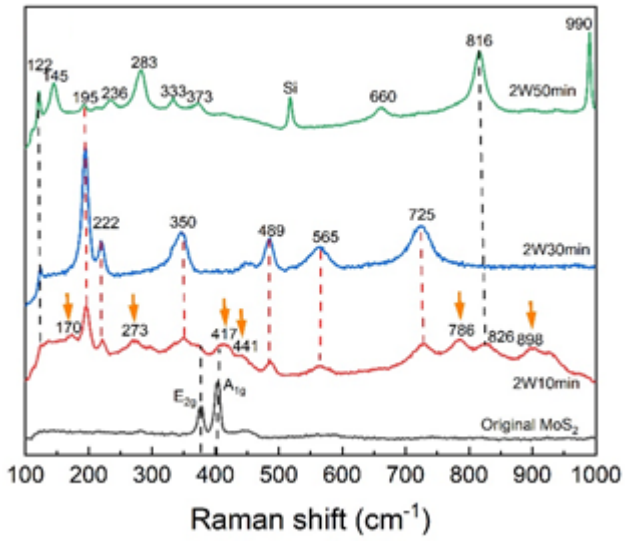

Figure 4.2 Raman spectra of untreated MoS_2 in black. MoS_2 is irradiated by the femtosecond laser for 10 minutes at 2W shown in red, 30 minutes at 2W in blue and 50 minutes at 2W in green. Dashed black lines indicated MoS_2 peaks. Dashed red lines indicated partially oxidized MoO_{3-x}. Orange arrows indicate H_xMoO_3.

XPS was also used to characterize the MoO_{3-x}. Figures 4.3a-d show the XPS spectra of the original MoS_2 powder and the samples after femtosecond laser treatment in 80% ethanol for 10, 30 and 50 minutes at 2W, respectively. In Figure 4.3a, there are three prominent peaks which correspond to sulphur 2s, molybdenum $3d_{5/2}$ and molybdenum $3d_{3/2}$ orbitals at 227, 229.8 and 233 eV, respectively. After the first 10 minutes of laser treatment, new peaks start to form which correspond to Mo(V) and Mo(VI) bonds as shown in Figure 4.3b. The Mo(V) and Mo(VI) peaks indicate that the MoS_2 is partially oxidized to form some substoichiometric molybdenum oxide. However the presence of the sulphur 2s and the Mo(IV) peaks still indicate a significant amount of MoS_2 present. After 30 minutes of laser treatment, both the sulphur 2s and the Mo(IV) peaks significantly decrease as shown in Figure 4.3c. This signifies that most of the MoS_2 has been partially oxidized. In addition there is an increase in Mo(VI) peaks suggesting that the majority of the material was MoO_{3-x}. Continuing to laser treat for 50 minutes causes the complete oxidation of the original MoS_2 material. As shown in Figure 4.3d, both the sulphur 2S and

Mo(IV) peaks are completely undetectable indicating that the MoS_2 had become fully oxidized to MoO_3. Furthermore, the Mo(VI) peaks have increased significantly while the Mo(V) peaks decrease further, consistent with the complete oxidation of MoO_3.

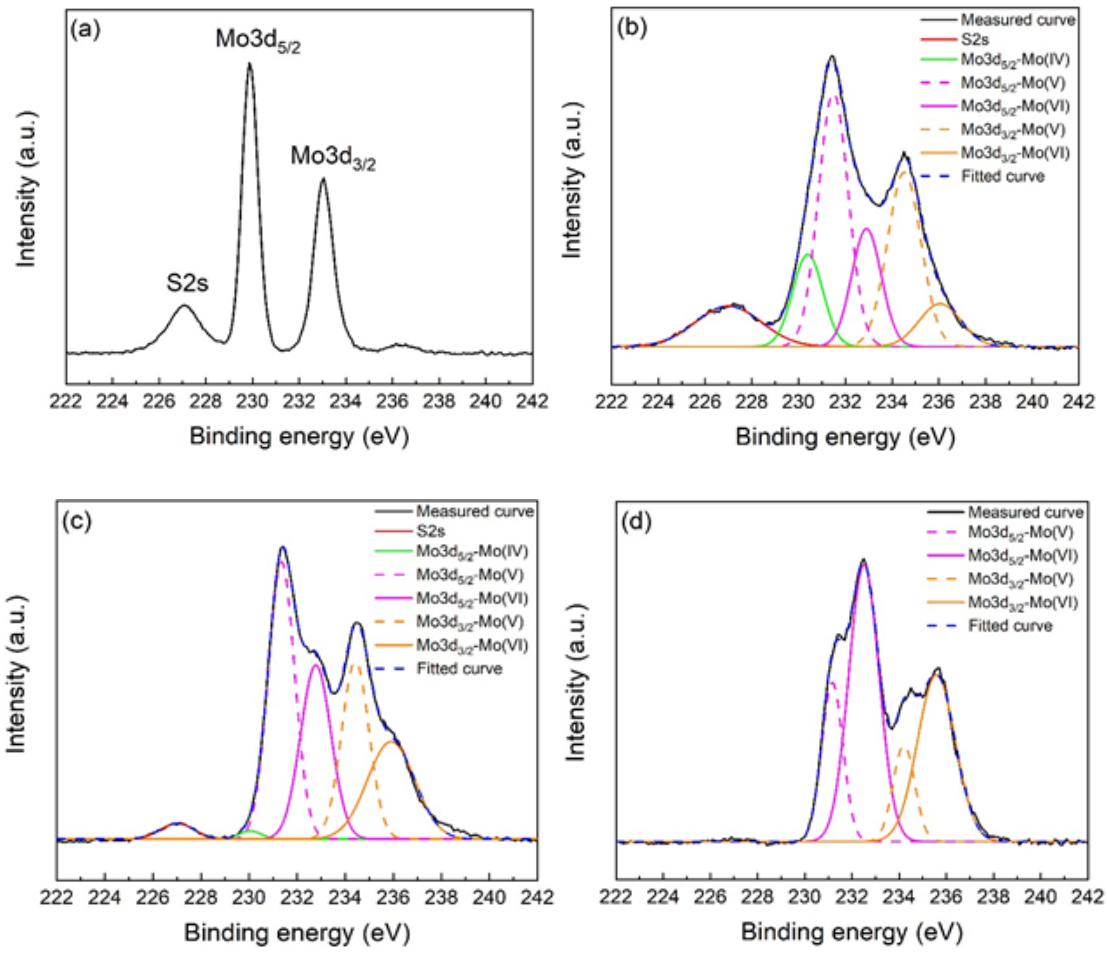

Figure 4.3 XPS spectra of (a) Untreated MoS_2 in 80% ethanol. (b) Femtosecond laser irradiated MoS_2 at 2W for 10 minutes in 80% ethanol. (c) Femtosecond laser irradiated MoS_2 at 2W for 30 minutes in 80% ethanol. (d) Femtosecond laser irradiated MoS_2 at 2W for 50 minutes in 80% ethanol.

Both the Raman and XPS data confirm that femtosecond laser irradiation can partially oxidize MoS_2 under the correct conditions. By dissolving MoS_2 powders in 80% ethanol in water and using a femtosecond laser to irradiate the nanoparticle solution at 2W for 30 minutes, MoO_{3-x} can be synthesized. Interestingly, different ratios of ethanol to water and femtosecond laser treatment

times affect the level of oxidation. In the following section, it will be shown that the level of oxidation influences the plasmonic photothermal conversion efficiencies of MoO_{3-x}.

4.2 Photothermal Measurements of Femtosecond Laser-Treated Molybdenum Disulfide

Photothermal conversion efficiency measurements of the laser-treated samples were taken using the PTCE system from Chapter 3. Two main sets of experiments were conducted to determine the effects on the PTCE. The first experiment involved changing the ratio of ethanol and water as the solvent. The second experiment involved altering the femtosecond laser treatment times to determine differences in the PTCE. To determine the PTCE, the absorbance spectrum for each sample was first measured. For the first experiment, the normalized absorbances of the laser-treated samples in solvents containing pure water, pure ethanol, and 30%, 70%, 75%, 80%, 85%, and 90% ethanol in water were measured and displayed in Figure 4.4a. These samples were laser treated at 2W for 30 minutes.

For the second experiment, the normalized absorbances of the laser-treated samples with varying laser treatment times (10, 20, 30, 35, 40 and 50 minutes) were measured and are displayed in Figure 4.4b. These MoS_2 samples were dissolved in 80% ethanol/water and were irradiated using a laser power of 2W.

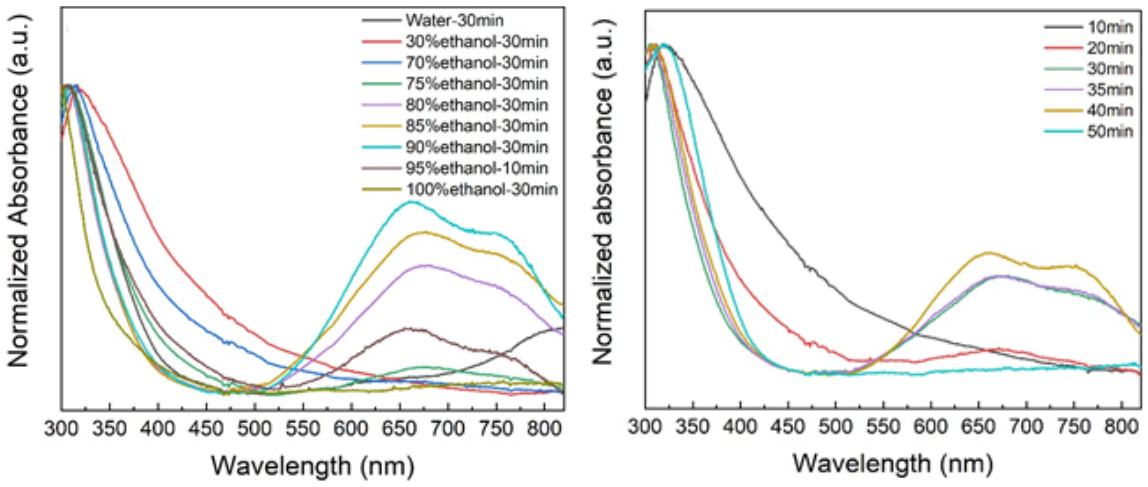

Figure 4.4 Absorbance spectra of (a) femtosecond laser-treated MoS_2 with varying ethanol concentrations (water, ethanol, and 30%, 70%, 75%, 80%, 85%, 90%, and 95% ethanol in water), (b) femtosecond laser-treated MoS_2 with varying laser irradiation times (10, 20,30,35,40 and 50 minutes).

From Figure 4.4a and b, a large plasmonic peak can be seen at around 675 nm and a smaller peak at around 750 nm for some samples. The appearance of the 675 nm peak can be seen in Figure 4.4a for the 75% ethanol-30min sample and in Figure 4.4b for the 20 minute sample. As the laser treatment continues to oxidize the MoS_2, another peak appears at 750 nm which indicates the formation of plasmonic nanomaterials, consistent with the results from Ref. [59]. For both sample sets, the plasmonic peaks continue to increase with femtosecond laser treatment time and ethanol concentration up to an extent. Once the percentage of ethanol is greater than 90%, the plasmonic peaks start to drop with the peaks being completely gone at 100% ethanol. Similarly, once the femtosecond laser treatment duration is longer than 40 minutes, the plasmon peak diminishes and completely disappears after 50 minutes. Therefore, both the femtosecond laser treatment time and ethanol concentration play a role in changing the optical properties.

Samples containing the plasmonic peaks are considered to be MoO_{3-x} due to the oxygen vacancies created by the solvent and femtosecond laser. Oxygen vacancies are the primary

reason for the plasmonic peaks found in each sample. Therefore, samples that contain between 75-95% ethanol-water are considered to be $MoO_{3-x.}$ Similarly, samples that are femtosecond irradiated between 20-40 minutes at 2W are also MoO_{3-x}, which is consistent with the Raman spectroscopy performed by Fan Ye (Figure 4.2 and Ref. [47]).

After determining the absorbance for each sample, the PTCE of each sample was measured. The results of the solvent-varied and time-varied experiments can be seen in Table 4.1 and 4.2, respectively. In both experiments, the highest PTCE value of 34% was found for an 80% ethanol in water solvent and 30 minutes of laser treatment at 2W.

Table 4.1 PTCE values of femtosecond laser irradiated MoS_2 with varying ethanol concentrations.

Solvent	**PTCE**	**Temperature Change (°C)**	**Absorbance at 808 nm**	**Time Constant τ_s**
Pure Water	13%	2.3°C	0.115	544s
30% Ethanol	33%	9.3°C	0.269	437s
70% Ethanol	32%	10.2°C	0.251	401s
75% Ethanol	33%	13°C	0.344	358s
80% Ethanol	34%	15.5°C	0.458	345s
85% Ethanol	33%	16.1°C	0.511	337s
90% Ethanol	32%	17.6°C	0.544	355s
95% Ethanol	33%	16.6°C	0.437	336s
100% Ethanol	15%	3.1°C	0.091	409s

Table 4.2 PTCE values of femtosecond laser irradiated MoS_2 with varying laser irradiation times.

Femtosecond Laser Time	**PTCE**	**Temperature Change (°C)**	**Absorbance at 808 nm**	**Time Constant τ_s**
No Laser	9%	5.5°C	0.211	338s
10 Minutes	27%	12.8°C	0.409	351s
20 Minutes	31%	14.2°C	0.399	353s
25 Minutes	33%	15.9°C	0.512	355s
30 Minutes	34%	15.5°C	0.458	345s
35 Minutes	32%	13°C	0.337	356s
40 Minutes	12%	4.5°C	0.213	407s
45 Minutes	12%	6.9°C	0.342	433s
50 Minutes	~0%	0.7°C	0.022	1114s

To ensure the photostability of the newly synthesized MoO_{3-x}, cyclic irradiation and non irradiation were done with the NIR laser to create a cyclic heating/cooling curve. This was repeated for 5 cycles as shown in Figure 4.5 to ensure consistent heating and cooling of the MoO_{3-x} material. From Figure 4.5, the 5 cycles are almost identical indicating that under NIR irradiation, the nanomaterial is stable. Therefore the femtosecond laser is able to create partially oxidized MoO_{3-x} from the starting multilayer MoS_2 with the addition of ethanol and water providing oxygen. Within the lattice structure of the MoO_{3-x} oxygen vacancies are exist causing the nanomaterial to have plasmonic properties. With the photostability of MoO_{3-x} shown in Figure 4.5, the nanomaterial is stable and will not further oxidize unless irradiated for longer times under the femtosecond laser.

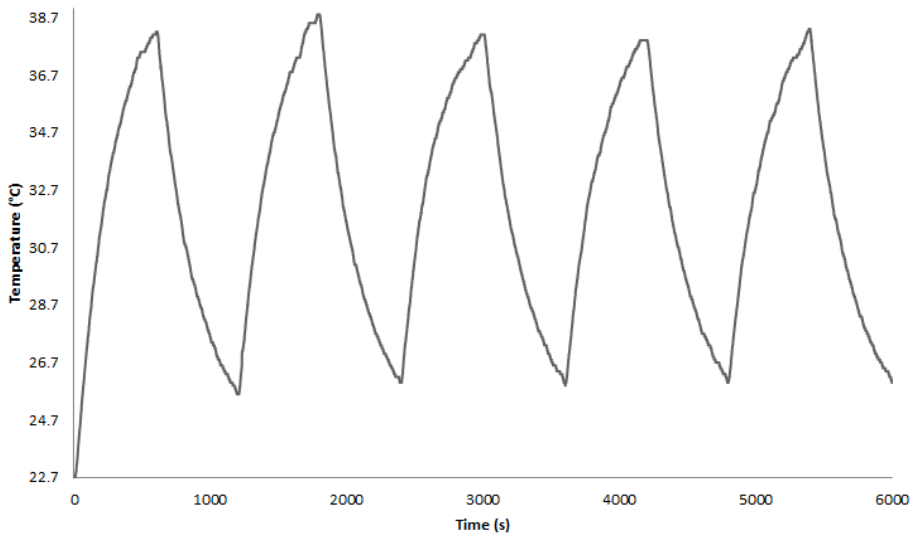

Figure 4.5 Photothermal stability of femtosecond laser-treated MoS_2

4.3 Discussion of Photothermal Properties of Plasmonic Substoichiometric Molybdenum Oxide

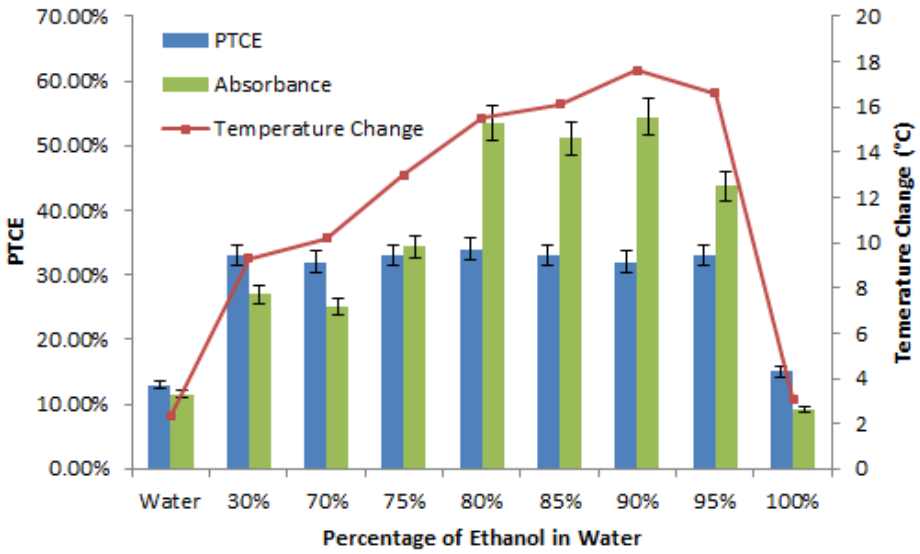

Figure 4.6 Photothermal conversion efficiencies, temperature changes and absorbances (808 nm) of femtosecond laser irradiated MoS_2 dissolved in various percentages of ethanol-water mixtures. The femtosecond laser had a power of 2W and each sample was irradiated for 30 minutes.

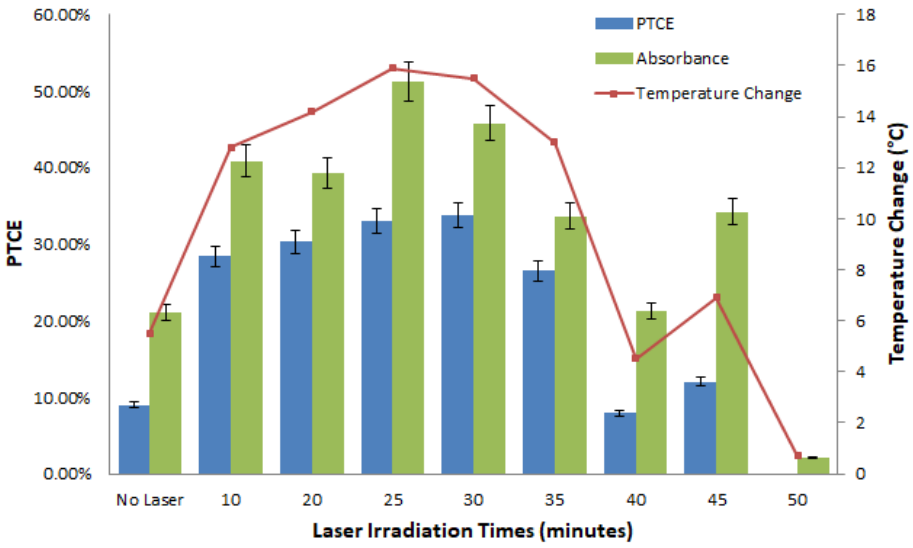

Figure 4.7 Photothermal conversion efficiencies, temperature changes and absorbances (808 nm) of femtosecond laser irradiated MoS_2 with varying laser irradiation times. The femtosecond laser had a power of 2W and an 80% ethanol solvent was used to dissolve the MoS_2.

Figures 4.6 and 4.7 show the measured PTCE, temperature change, and absorbance at 808 nm of the laser-treated MoS_2 as a function of the percentage of ethanol in the solvent and the irradiation time, respectively. Trends can be clearly seen. In both experiments, the highest PTCE value was obtained for 80% ethanol and 2W for 30 minutes. However, an even higher PTCE value was found for another femtosecond laser-treated MoS_2 sample with a solvent containing 95% ethanol that was laser treated at 2W for 25 minutes. It had a PTCE value of 40% and absorbance of 0.512 at 808 nm. The temperature change and time constant fit derived from the cooling curve for that sample can be seen in Figure 4.8a and b respectively.

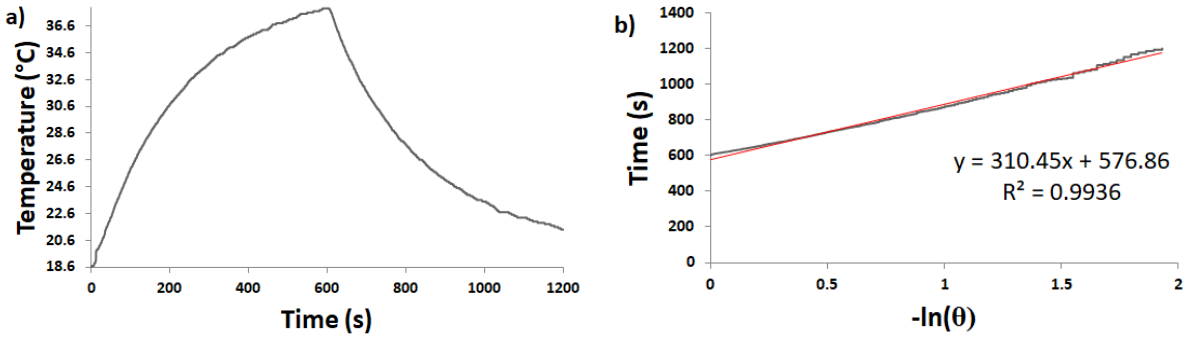

Figure 4.8 Femtosecond laser-treated MoS_2 in 95% ethanol, laser-treated 2W for 25 minutes. (a) Temperature change curve of laser-treated sample (b) Time constant fit curve with a time constant of 310 seconds.

4.3.1 Effects of Ethanol and Water

To understand the photothermal behavior of the plasmonic molybdenum oxide, the role of both water and ethanol must be considered. Observed in the absorbance spectra in Figure 4.4, only samples with greater than 70% ethanol exhibited localized surface plasmon resonance (LSPR) peaks. As the concentration of ethanol increased, the LSPR also increased up to a maximum of 90% and then sharply decreased to no LSPR peaks at 100% ethanol. The lack of LSPR peaks at 100% ethanol is due to the complete oxidation to MoO_3, as found from the Raman spectroscopy done by Fan Ye (Figure 4.2 and Ref. [47]), which resulted in very poor absorbance at 808 nm. Oxygen vacancies are primarily responsible for the plasmonic effects seen in the MoO_{3-x}. Therefore, the lack of oxygen vacancies causes the lack of LSPR peaks which resulted in a weaker photothermal effect such that the PTCE and temperature change were lower in comparison to the other samples. However, even though the 30% ethanol sample displayed no LSPR peaks in Figure 4.4, it had a relatively good absorbance and photothermal effect indicating that both ethanol and water are required in a mixture to be able to create plasmonic MoO_{3-x}. It is expected that the relative amounts of ethanol and water influence the concentration of oxygen

vacancies. The amount of oxygen vacancies has an effect on the plasmonic characteristics of MoO_{3-x} such that only phases with $0.125 < x < 1$ have enough free electrons to demonstrate metallic characteristics [60]. Due to higher LSPR peaks seen in samples with higher ethanol concentrations, it can be concluded that ethanol has a significant influence on the concentration of oxygen vacancies. In order for LSPR to occur, the dielectric constant of the nanoparticles must be negative [61]. Since water has a higher dielectric constant compared to ethanol (79.99 versus 25.02 respectively [62]), it is unable to facilitate a negative dielectric constant which explains the lack of LSPR peaks. However, water is still able to produce enough oxygen vacancies to create a substoichiometric MoO_{3-x} with $x > 0.125$. Another observation to note is the red shift in absorbance for the pure water sample indicating plasmonic peaks that have been shifted to a longer wavelength. Due to pure water having a higher dielectric constant, the LSPR peak will tend to red shift [63] causing a lower absorbance at 808 nm which results in a weaker photothermal effect, as shown in Table 4.1 and Figure 4.6. It It is expected that water plays a crucial role in releasing $-OH_2$ groups from H_xMoO_3 because it forms stronger hydrogen bonds compared to ethanol, which ultimately facilitates the creation of oxygen vacancies and MoO_{3-x}, such that absorbance and PTCE are highest when some water is present in the solvent.

From the experimental data from Table 4.1, it appears that the plasmonic MoO_{3-x} have greater absorbance, temperature increases and a quicker time constant seen in samples with between 80-95% ethanol concentrations. Higher absorbances usually indicate that the nanomaterial is absorbing the NIR light. Conversely, the higher the temperature change, the better the light is converted into heat for a fixed absorbance. The time constant indicates the cooling rate of the sample after the NIR laser is turned off. Smaller time constants indicate that the sample cools

faster which means that the material exchanges heat at a faster rate. The importance of each parameter is observed in the variety of PTCE values of each sample.

Overall, both water and ethanol play an important role in creating substoichiometric plasmonic MoO_{3-x} with ethanol having a greater influence on the plasmonic LSPR peaks and water affecting the release of $-OH_2$ groups from H_xMoO_3. This creates a material with strong photothermal properties with high PTCE values.

4.3.2 Femtosecond Laser Tuning via Time and Power

The femtosecond laser treatment time also has a significant effect on the photothermal behavior of the MoO_{3-x}. From Table 4.2 and Figure 4.7, the optimal femtosecond laser irradiation time is between 20 to 30 minutes. With only 10 minutes of laser at 2W, there is enough energy to break down the MoS_2 bulk powder and start the oxidation process. However, as observed in the absorbance curves in Figure 4.4 b, true LSPR peaks do not form until around 20 minutes, suggesting that there is still a significant amount of MoS_2 remaining. Nevertheless, the start of the oxidation process at 10 minutes is still able to create a photothermal response as seen in Figure 4.7. As the femtosecond laser irradiation time increases the partial oxidation and plasmonic peaks increase as well until reaching a maximum at 30 minutes, at which point the plasmonic peaks disappear as the MoS_2 is fully oxidized to MoO_3.

The data in Figure 4.7 follows this general trend of increasing PTCE, absorbance and temperature change as the irradiation time increases. However, during the photothermal testing under the NIR laser, the 40 minute sample changed color from a light blue to clear. This clear color was similar to the 45 and 50 minute samples which suggests that the 40 minutes sample

had completely oxidized in atmospheric conditions. The result is poor photothermal performance as a result of a much lower absorbance at 808 nm.

Different femtosecond laser powers were tested for the creation of plasmonic MoO_{3-x}, however it appears that only 2W is able to create a solution that is visibly blue indicating the creation of substoichiometric molybdenum oxide. Higher and lower laser powers only created clear or brown solutions. This is most likely due to lower laser powers not having enough energy to begin oxidizing the MoS_2 resulting in a brown solution and higher laser powers fully oxidizing the MoS_2 to MoO_3 resulting in a clear solution.

Hence, it was found that both femtosecond irradiation time and power play important roles in the creation of plasmonic substoichiometric molybdenum oxide. The femtosecond laser time must be within a certain range when irradiated at 2W. It is possible that a different femtosecond laser power can also create plasmonic substoichiometric molybdenum oxide; however, the laser irradiation time should be adjusted to compensate. More specifically if a higher laser power is used, then a shorter irradiation time is required and vice versa.

4.3.3 Effects of Solar Simulation

Alsaif et al. were able to tune the plasmonic resonance of MoO_3 with the assistance of artificial sunlight [64]. The MoO_3 was converted into molybdenum bronze (H_xMoO_3) by intercalating the van der Waal gaps in the 2D MoO_3 layers with ions taken from water. As the ions leave, they strip away oxygen from the lattice creating MoO_{3-x}. This process of creating molybdenum bronze requires water and sunlight and is shown in Equations (18),(19) and (20) [65].

$$MoO_3 \rightarrow MoO_3^* + h^+ + e^- \qquad (18)$$

$$2h^+ + H_2O \rightarrow 2H^+ + \frac{1}{2}O_2 \qquad (19)$$

$$MoO_3 + xH^+ + xe^- \rightarrow H_xMoO_3 \qquad (20)$$

Essentially, during solar irradiation an electron-hole pair forms which causes the release of H^+ ions from the H_2O. The H^+ ions intercalate the MoO_3 layers and create the $-OH_2$ groups attached to H_xMoO_3 [66]. As the oxygen is stripped away from the H_xMoO_3 lattice, a substoichiometric MoO_{3-x} is formed.

With this information, a solar simulator was used to irradiate the fully oxidized MoO_3 from the previous experiments. A femtosecond laser-treated sample at 2W for 35 minutes of MoS_2 in ethanol had fully oxidized to MoO_3 due to being exposed to the atmosphere for a prolonged period of time, as indicated by the clear color of the solution and a weak photothermal performance. The MoO_3 sample was irradiated using a Sciencetech solar simulator with simulated AM1.5 sunlight at an intensity of ~100 mW/cm^2 for two hours. It was found that the MoO_3 could be reversed back to substoichiometric molybdenum oxide, presumably by a process similar to that reported by Alsaif et al. Figure 4.9a-c shows the heating/cooling, absorbance spectra and time constant fit data for the sample before and after the solar illumination. An improved photothermal performance is observed and the solution was observed to change to a blue color, indicating the presence of MoO_{3-x}. With the improvement of photothermal heating, the PTCE increased significantly from ~5% to 33%.

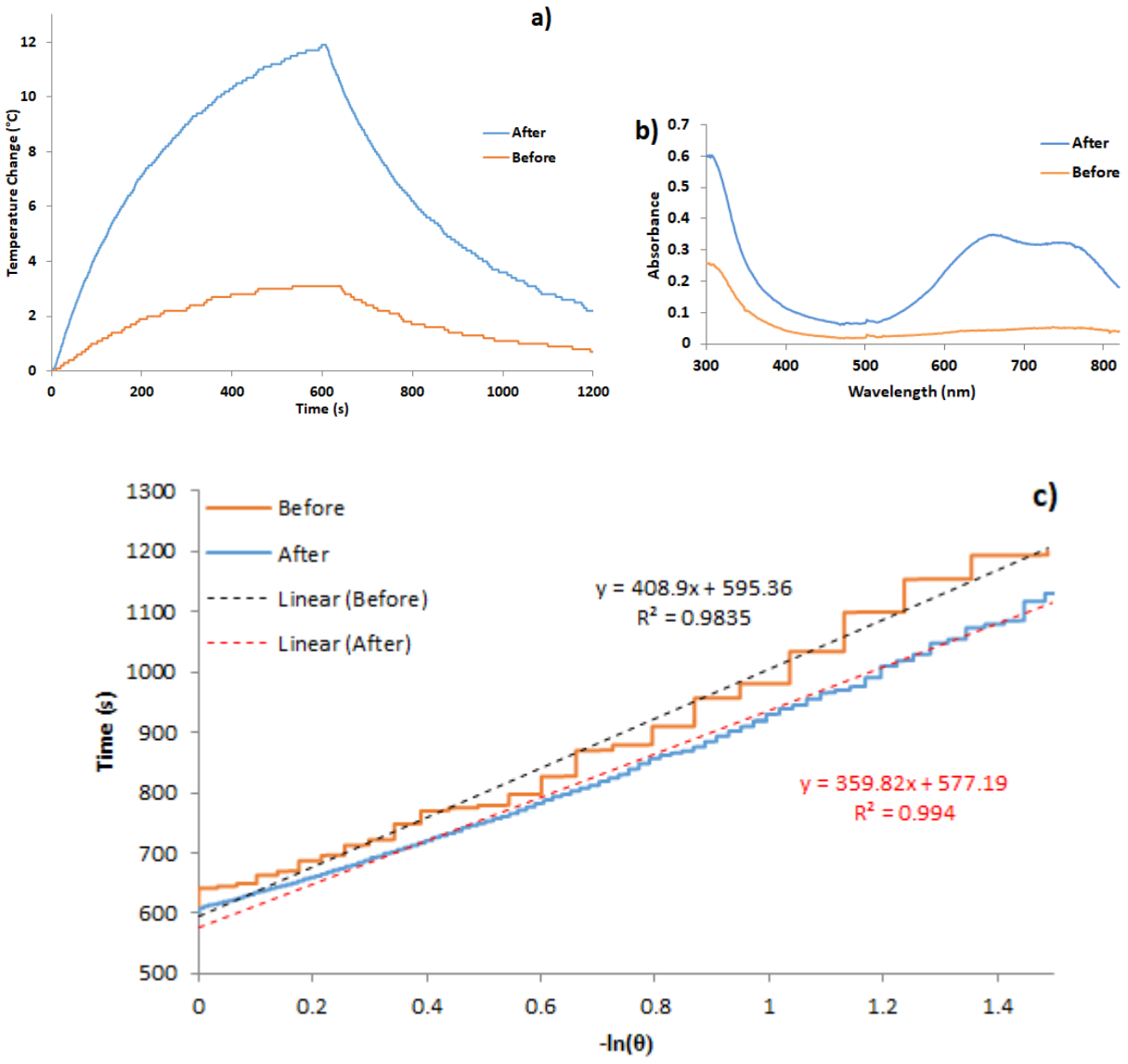

Figure 4.9 Comparison of temperature increases due to NIR light photothermal conversion of solar irradiated MoS_2 compared to without solar irradiation. (a) Temperature changes before and after solar irradiation (b) Absorbance spectra before and after solar irradiation (c) Time constant fit plot before and after solar irradiation with time constants 409s and 360s respectively.

Overall, solar irradiation has the ability to influence the chemistry of the nanomaterial which ultimately affects the photothermal properties. By utilizing the catalytic effects of solar light on water, it may be possible to enhance the photothermal properties of MoO_{3-x} by creating more H^+ ions to form $-OH_2$ groups that bond to H_xMoO_3. This will allow water to play a larger role in creating MoO_{3-x} and combined with ethanol, it is possible to create a better photothermal agent.

Chapter 5 Photothermal Agent: Tungsten Semi-carbide

5.1 Synthesis of Two Dimensional Tungsten Semi-carbide via the Carbonization of Tungsten Disulfide

In this chapter, the synthesis of 2D tungsten semi-carbide (W_2C) by direct carbonization of 2D tungsten disulfide using femtosecond laser irradiation is studied. Current synthesis methods of tungsten-carbon compounds, including tungsten carbide (WC) and tungsten semi-carbide (W_2C), require high temperature processes such as vacuum sintering, atmospheric carburization, ball milling and plasma [67]. One of the advantages of carburizing tungsten disulfide into tungsten semi-carbide is the ability to maintain the two dimensional structure of tungsten disulfide. Tungsten carbide is known to have been synthesised from tungsten disulfide as the starting material in order to create a high surface area material capable of electrocatalytic hydrogen oxidation [68]. Hara et al. synthesized tungsten carbide (WC) [69] directly by carburizing WS_2 as shown in Equation (21), however tungsten semi-carbide (W_2C) could only be synthesized using tungsten oxide (WO_3) as the starting material [68] as seen in Equation (22). Both processes required carburization at high temperatures of 900K and required 5 hours to complete.

$$WS_2 + CH_4/H_2 \rightarrow WC \qquad \mathbf{(21)}$$

$$WO_3 + C_2H_6/H_2 \rightarrow W_2C \qquad \mathbf{(22)}$$

Thus, a novel, faster, room-temperature synthesis method using the same starting material was created using a femtosecond laser. To begin, 0.25 mg/ml of tungsten disulfide powder was

dissolved in acetonitrile. An ultrasonic bath in combination with the acetonitrile solvent assisted in breaking up the powder and separating the WS_2 layers held together by weak van der Waals forces. Although the bulk WS_2 flakes were suspended in the acetonitrile, giving a uniform distribution, the WS_2 flakes were not completely dissolved and aggregated over time if unperturbed. Next, the WS_2 solution was irradiated by a femtosecond laser which further separates the WS_2 layers and breaks down the solvent (laser irradiation performed by Fan Ye). Laser powers ranging from 0.2 to 4 W and laser times from 10 to 45 minutes were used. The solvent is disassociated due to the Coulomb explosion induced by the ultrafast femtosecond laser which generates methyl functional groups. At the same time, the W-S bonds are broken, creating bonding sites for the energetically favoured carbon molecules to attach [70]. Thus the carbonization of WS_2 occurs via the femtosecond laser irradiation. The shape is expected to be similar to the 2D WS_2 with the exception of carbon replacing the sulfur atoms. The expected synthesis process can be seen in Figure 5.1 which demonstrates the carburization of WS_2.

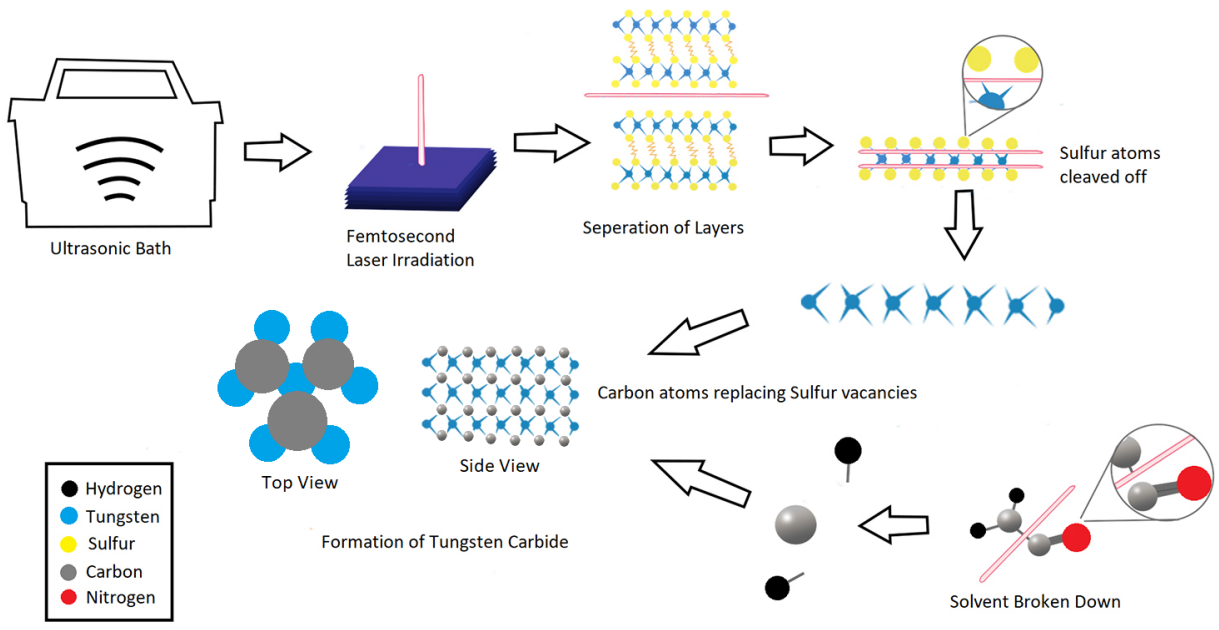

Figure 5.1 Synthesis overview of tungsten semi-carbide via femtosecond laser irradiation.

5.2 Characterization of Two Dimensional Tungsten Carbide

In order to confirm the synthesis of two-dimensional tungsten semi-carbide, GIXRD, SEM, energy dispersive x-ray analysis (EDX), XPS, AFM and Raman spectroscopy were performed. It is important to note that the measurements were provided by Fan Ye and the technicians at WATLab. GIXRD was performed using the PANalytical X'pert Pro MRD and was used to identify the phase of the material. XPS was performed using the Thermo VG ESCALab 250 and was used to determine the surface elemental composition in addition to the types of molecular bonds. AFM was performed using the DI Nanoscope IV and was used to visualize the nanoparticle morphology and determine the average sizes. SEM was performed using a Zeiss FESEM 1530 to visualize the morphology of the nanoparticles in addition to providing an elemental composition using EDX. Raman spectroscopy was performed using a Renishaw Ramascope dual-wavelength micro-Raman spectrometer and was used to compare various vibrational modes corresponding to different types of bonds.

5.2.1 Grazing Incidence X-Ray Diffraction

Figure 5.2a shows GIXRD data for a tungsten disulfide sample that was irradiated for 40 minutes at 0.4 W. The nanoparticle solution was dropped onto a silicon wafer for analysis. For comparison, untreated tungsten disulfide powder was also scanned and is shown in Figure 5.2b.

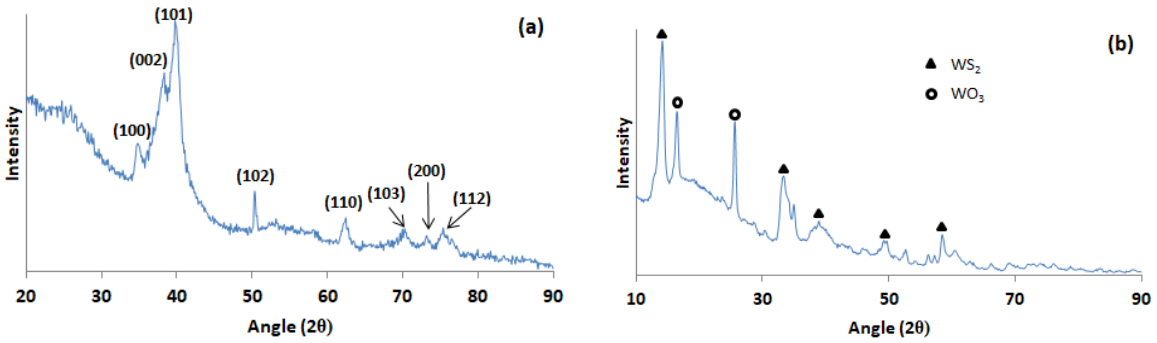

Figure 5.2 GIXRD data of (a) femtosecond laser-treated WS_2 (40 minutes at 0.4 W), (b) untreated WS_2 powder.

It is clear that the femtosecond laser treatment has changed the structure of the material. Using Panalytical Highscore software, the femtosecond laser treated sample had a strong match with JCPDS card 00-035-0776 for tungsten semi-carbide (W_2C), as shown in Figure 5.2a. Surprisingly, the tungsten disulfide powder was found to actually be a mixture of both tungsten disulfide (WS_2) and tungsten oxide (WO_3) as shown in Figure 5.2b. This can be attributed to the natural oxidation of WS_2 powder exposed to atmospheric conditions over time.

From the GIXRD data, eight prominent matching peaks were determined as seen in the blue lines in Figure 5.2a. These peaks were found at 34.76°, 38.06°, 39.86°, 50.35°, 62.33°, 70.22°, 73.07° and 75.22° which correspond to the (100), (002), (101), (102), (110), (103), (200) and (112) planes of W_2C, respectively.

Using a crystal geometry equation for hexagonal crystal systems shown in Equation (1), the lattice parameters for W_2C were calculated from the planes found in Figure 5.2a. The calculated lattice parameters are compared to the values in the JCPDS card in Table 5.1 and match well.

$$\frac{1}{d^2} = \frac{4}{3}\left(\frac{h^2 + hk + k^2}{a^2}\right) + \frac{l^2}{c^2} \qquad (23)$$

Where *h*, *k* and *l* are the miller indices of the planes, *d* is the interplanar spacing and *a* and *c* are the lattice constants of the unit cell.

Table 5.1 Calculated lattice parameters compared to JCPDS database lattice parameters

Lattice Parameters	**JCPDS Card**	**Calculated**
a	2.997 Å	2.988 Å
b	2.997 Å	2.988 Å
c	4.7279 Å	4.7248 Å

Using the Scherrer equation shown in Equation (2), an approximation of the average crystallite size can be determined from the GIXRD data.

$$D = \frac{K\lambda}{\beta cos(\theta)} \qquad (24)$$

Where *D* is the average crystallite size, *K* is the Scherrer constant, λ is the x-ray wavelength, β is the full width at half max (FWHM) of the peak and θ is the peak position. Taking each of the eight peaks identified by the GIXRD, Table 5.2 shows the average crystallite sizes for each peak. Note that the Scherrer constant is taken to be 0.9 and the x-ray wavelength is 0.154 nm. From Table 5.2, the crystallite sizes range from ~4-30 nm.

Table 5.2 Calculated crystallite sizes and interplanar spacings based on the GIXRD peak position and FWHM.

Peak (2θ)	**FWHM (rad)**	**Crystallites Size (nm)**	**Miller Indices (h k l)**	**Interplanar Space (Å)**
34.76°	0.799	10.42	(1 0 0)	2.58
38.06°	2.397	3.51	(0 0 2)	2.36
39.86°	1.598	5.29	(1 0 1)	2.26
50.35°	0.299	29.29	(1 0 2)	1.81
62.33°	0.699	13.28	(1 1 0)	1.49
70.22°	0.799	12.15	(1 0 3)	1.34
73.07°	0.599	16.49	(2 0 0)	1.29
75.22°	0.898	11.16	(1 1 2)	1.26

Overall, the GIXRD confirms the effectiveness of utilizing the femtosecond laser to change tungsten disulfide (WS_2) into tungsten semi-carbide (W_2C). It is also a possibility that the WS_2 was first oxidized to tungsten oxide (WO_3) before being carburized to W_2C by the femtosecond laser. Contribution from both WS_2 and WO_3 in addition to the acetonitrile may result in the synthesis of W_2C.

5.2.2 Atomic Force Microscopy

An atomic force micrograph of the same femtosecond laser irradiated WS_2 sample (0.4 W for 40 minutes) is shown in Figure 5.3. In initial measurements numerous aggregates were observed that formed due to the drop casting of the femtosecond laser-carburized W_2C on a silicon wafer. To remedy this, a 200 nm syringe filter was used to filter out the agglomerates. Figure 5.3 shows an AFM image of the femtosecond laser-carburized W_2C particles after being filtered. After selecting 189 particles, particle diameter and height histograms were determined, as shown in

Figure 5.4a and b respectively. Table 5.3 shows the average size distribution of the 189 particles selected giving insight on the morphology and dimensions of the nanoparticles.

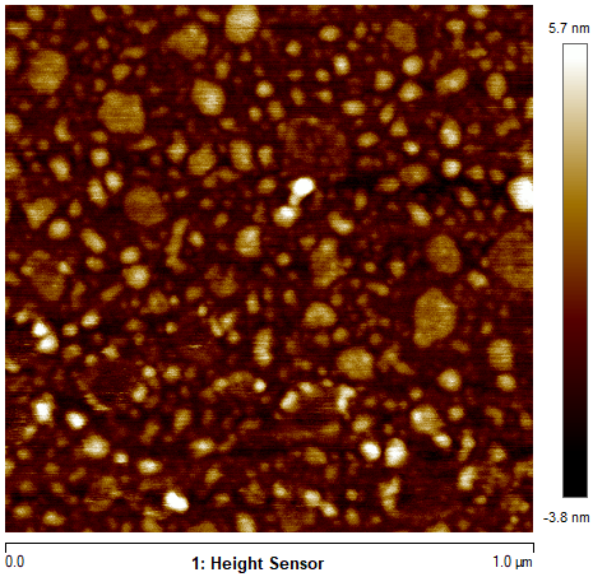

Figure 5.3 AFM micrograph of femtosecond laser-carburized W_2C at 0.4W for 40 minutes after a 200 nm filter is applied.

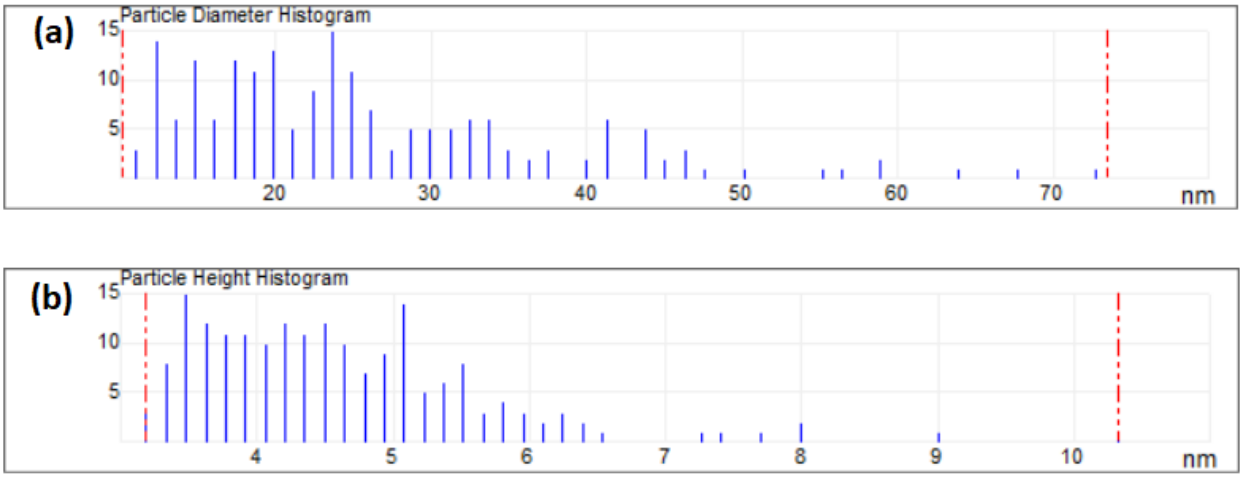

Figure 5.4 AFM histogram of (a) particle diameter distribution and (b) particle height distribution. Performed on femtosecond laser-carburized W_2C at 0.4W for 40 minutes.

Table 5.3 AFM size distribution of femtosecond laser-carburized W_2C at 0.4W for 40 minutes.

Particle Dimensions	Average	Minimum	Maximum
Diameter (nm)	26	11	73
Height (nm)	5	3	10
Area (nm^2)	632	95	4162

From Figure 5.4a and b in addition to Table 5.3, there is a wide distribution of particle sizes with the average diameter around 26 nm. The average height of 5 nm indicates that the particles are multilayer and confirms that the 2D morphology is maintained . The nanoparticles have a nanodisc-like shape due to the large diameter to height ratio. From Figure 5.3, the nanoparticles are shaped crudely like discs hence the nanodisc nomenclature.

Overall, AFM reveals the 2D nature of the W_2C nanodiscs in addition to providing approximate dimensions of the material. The 2D nature of the nanodiscs agrees with results found in the SEM images in the next section, which show that the morphology of the WS_2 powder appears to be unchanged as it undergoes femtosecond laser treatment.

5.2.3 Scanning Electron Microscopy & Energy Dispersive X-Ray Analysis

Samples were again drop-cast on silicon substrates for SEM analysis. SEM images are shown in Figure 5.5a-b and c-d for the untreated WS_2 and the femtosecond laser-carburized W_2C (40 minutes at 0.4W), respectively.

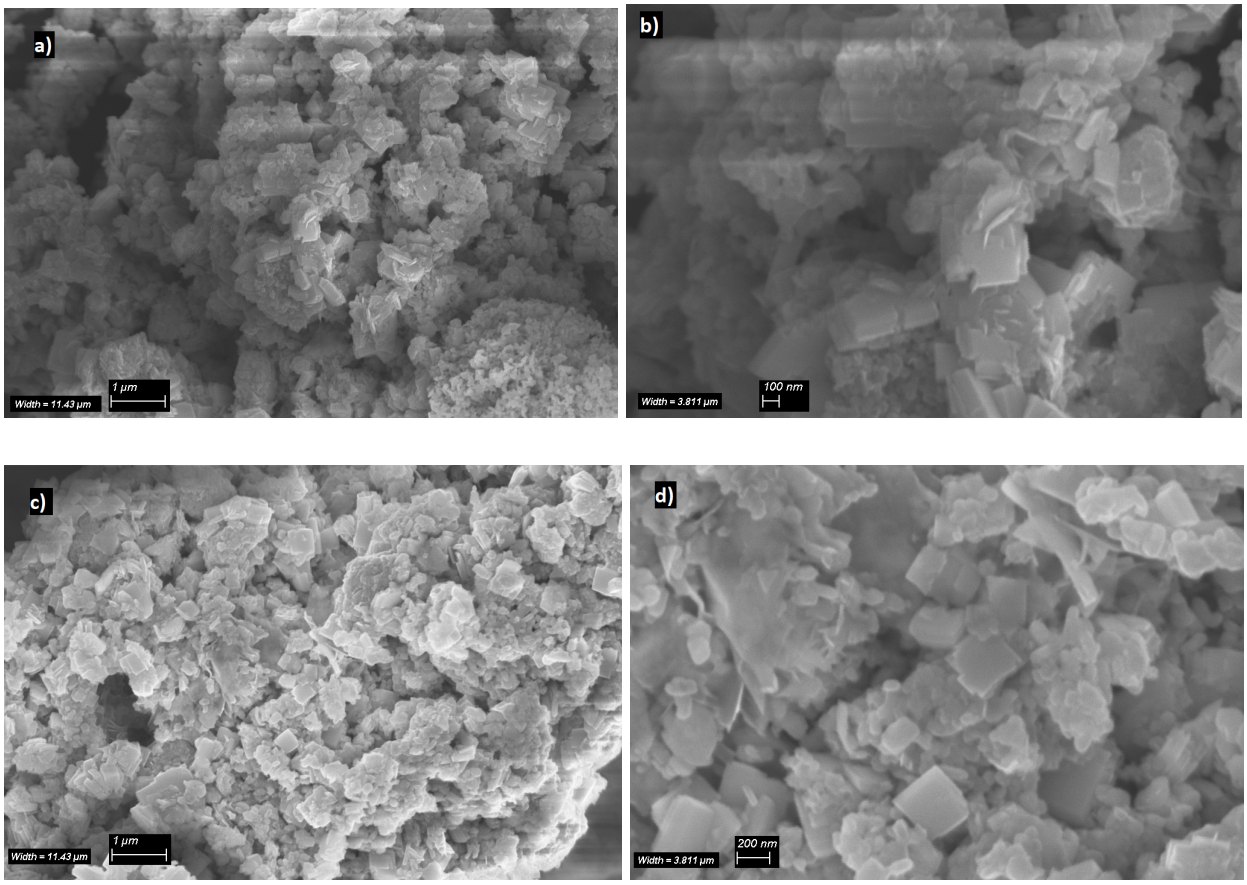

Figure 5.5 SEM images of (a) untreated WS_2, (b) zoomed in image of untreated WS_2, (c) femtosecond laser-carburized W_2C at 0.4 W for 40 minutes, (d) zoomed in image of femtosecond laser-carburized W_2C at 0.4 W for 40 minutes.

From the SEM images, the physical morphology of the laser-carburized W_2C is similar to that of the untreated WS_2. Aggregates consisting of flakes approximately 100-200 nm in size are observed in both images. This indicates the consistencies of the two dimensional morphologies between both materials. More specifically the flakes maintain the same shape after irradiating with a femtosecond laser and changing the chemical composition from WS_2 and WO_3 to W_2C. EDX characterization for both laser treated (40 minutes and 0.4 W) and non-laser-treated WS_2 is shown in Figure 5.6a and b respectively. The EDX spectrum for a sample treated with a higher laser power (40 min at 1.3 W) is shown in Figure 5.6c. The elemental composition for each sample is shown in Table 5.4.

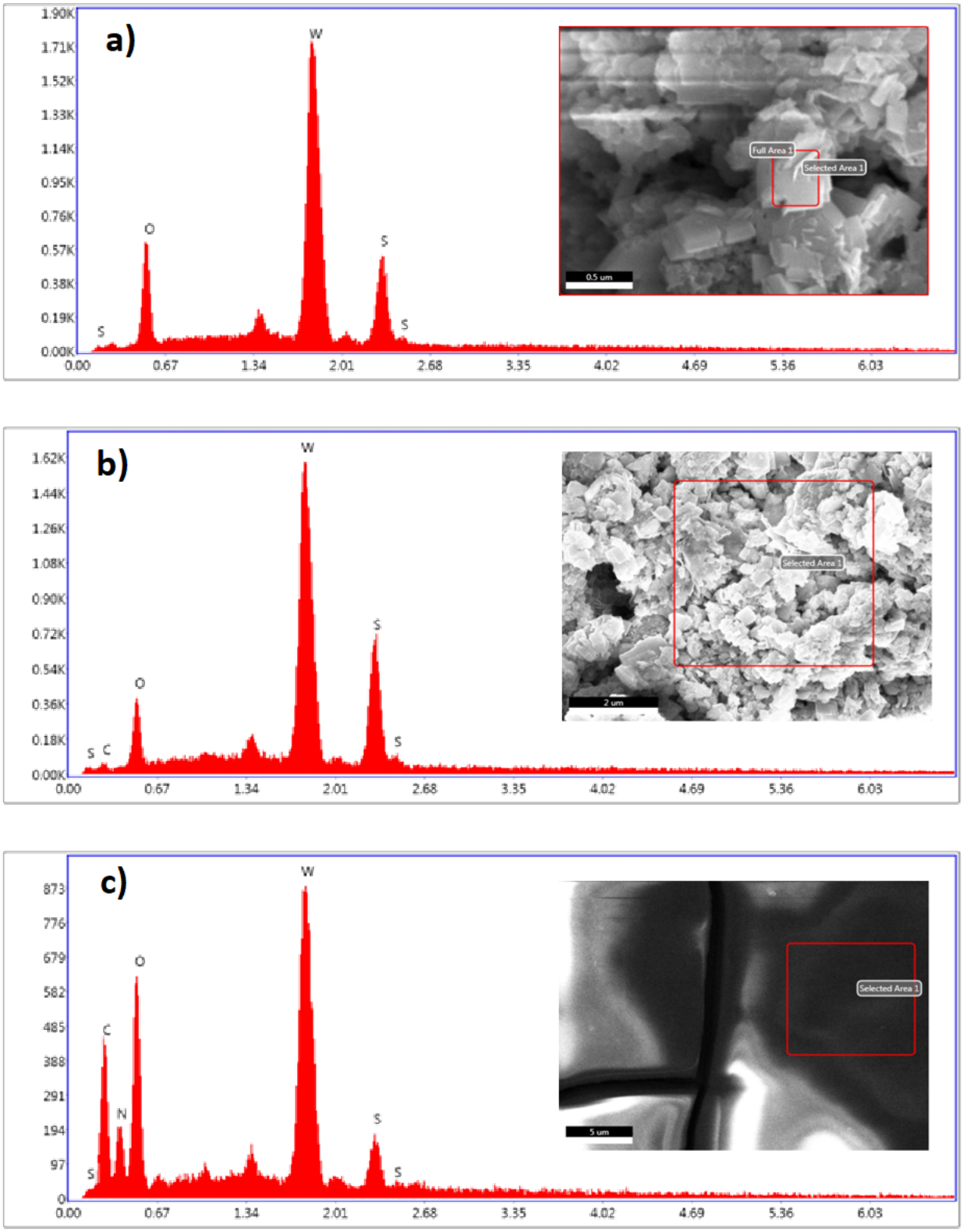

Figure 5.6 EDX results of (a) Non-laser irradiated WS_2. (b) Femtosecond irradiated WS_2 at 0.4W for 40 minutes. (c) Femtosecond irradiated WS_2 at 1.3W for 40 minutes.

Table 5.4 EDX elemental composition percentages of non-laser irradiated WS_2, femtosecond irradiated WS_2 at 0.4W for 40 minutes and femtosecond irradiated WS_2 at 1.3W for 40 minutes.

Element	**Non-Irradiated WS_2**		**Femtosecond Irradiated WS_2** (0.4W for 40 Minutes)		**Femtosecond Irradiated WS_2** (1.3W for 40 Minutes)	
	Weight %	**Atomic %**	**Weight %**	**Atomic %**	**Weight %**	**Atomic %**
Nitrogen	-	-	-	-	14.79%	24.26%
Carbon	-	-	3.9%	16.3%	19.53%	37.36%
Oxygen	15.77%	54.05%	10.51%	32.97%	21.17%	30.41%
Tungsten	69.5%	20.73%	64.44%	17.6%	40.46%	5.06%
Sulfur	14.74%	25.21%	21.15%	33.12%	4.06%	2.91%

From the elemental composition shown in Figure 5.6a-c and Table 5.4, there are significant changes. The oxygen content is reduced from 54% to 30% as a result of increasing the femtosecond laser power. This may be due to the removal of functional groups containing oxygen found on the surface of the WS_2 and the reduction of WO_3. Ibrahim et al. have shown that the femtosecond laser is able to remove oxygen containing functional groups from graphene oxide to create reduced graphene oxide [90]. There is also the introduction of a significant carbon peak which is consistent with the GIXRD results indicating the synthesis of W_2C from WS_2. However the EDX results indicate that the sulfur and oxygen contents are higher than carbon, which contradicts the GIXRD results. The differences can be attributed to the characterization methods in which GIXRD observes the crystal structure while EDX determines the elemental composition. Due to the samples being drop casted onto a silicon wafer, it is possible that sulfur compounds found in the solvent after being removed from the lattice by the femtosecond laser adhere to the wafer and appear in the EDX results. Therefore the true crystal

structure of the nanoparticles determined by GIXRD shows that W_2C is formed. The composition of the untreated WS_2 nanopowders (Table 5.4) is consistent with the GIXRD data, as the starting material was determined to be both WS_2 and WO_3 due to oxidation. The presence of both oxygen and sulfur peaks confirm that the untreated WS_2 samples were oxidized even before femtosecond laser treatment.

The elemental compositions shown in Table 5.4 indicate that oxygen is replaced with carbon atoms. Based on the relative weight and atomic percentages, it is clear that oxygen percentages significantly decrease as the partially-oxidized WS_2 powder is femtosecond laser treated. However, after using the femtosecond laser to irradiate another WS_2 sample using a higher power at 1.3 W instead of 0.4W, the EDX results in Figure 5.6c show that much of the sulfur peak has decreased and has been replaced by carbon, oxygen and nitrogen.

This indicates that as the femtosecond laser power is increased, there is a greater effect of both carburization and oxidation along with some degree of nitrogen doping. The carbon and nitrogen sources are from the acetonitrile solvent while the oxygen may come from both the oxidized WS_2 powder and the atmospheric oxygen.

Overall, the SEM and EDX characterization results show that the 2D morphology of the material can be maintained during the carburization process. For a laser treatment power of 0.4 W, carbon atoms are introduced and oxygen atoms are removed. For a higher femtosecond laser power of 1.3 W, additional small amounts of nitrogen atoms are incorporated from the acetonitrile solvent, while the amount of sulfur atoms decreases as more carbon, oxygen and nitrogen atoms replace them.

5.2.4 X-Ray Photoelectron Spectroscopy

The x-ray photoelectron spectrum of the femtosecond laser-treated-WS_2 is shown in Figure 5.7. The same sample used in GIXRD, SEM and EDX was also used for XPS. The femtosecond laser irradiation time was 40 minutes and the power was 0.4W. Figure 5.7 shows a survey scan and Table 5.5 provides atomic percentages, which are compared to the atomic percentages found from the EDX results.

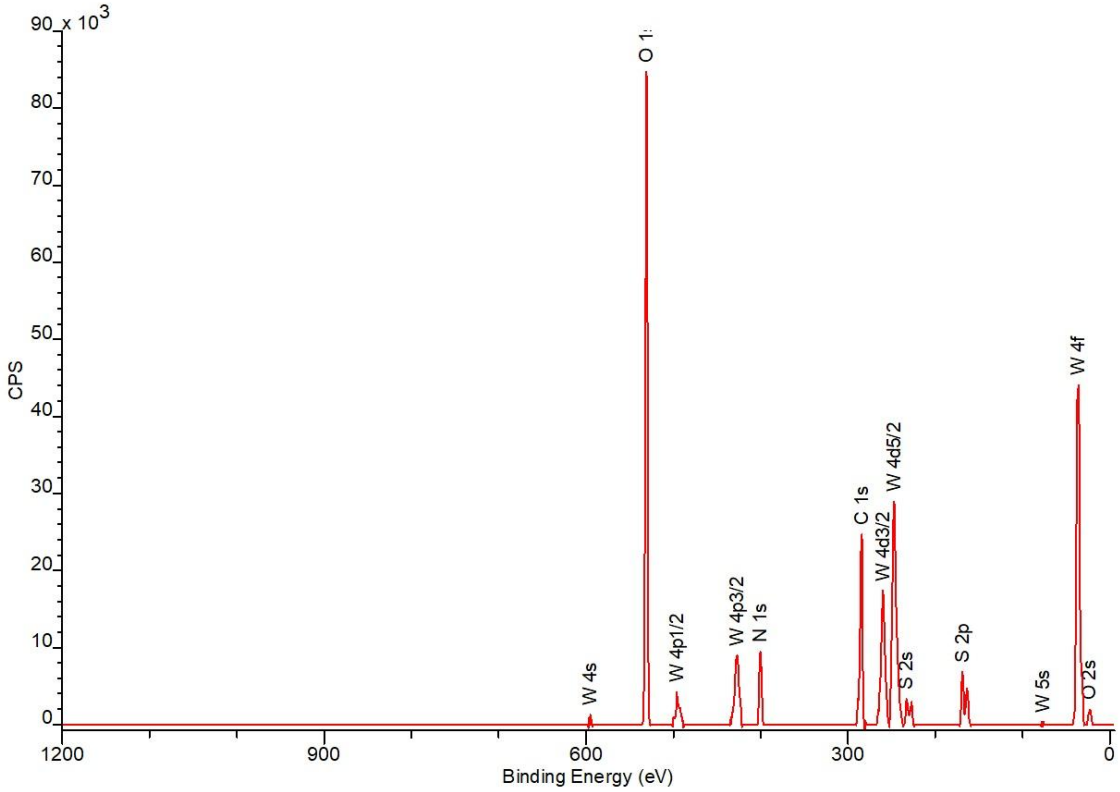

Figure 5.7 XPS Survey scan of femtosecond laser-carburized W_2C at 0.4W for 40 minutes.

Table 5.5 XPS elemental composition of femtosecond laser-carburized W_2C at 0.4W for 40 minutes in acetonitrile.

Element	Atomic Percentage (XPS)	Atomic Percentage (EDX)
Oxygen	38.75%	32.97%
Carbon	23.65%	16.3%
Nitrogen	5.18%	-
Tungsten	21.93%	17.6%
Sulfur	10.49%	33.12%

From the XPS survey scan, the presence of oxygen, carbon, nitrogen, tungsten and sulfur are as expected. The atomic percentages of both the XPS survey scan and the EDX results show some similarities in percent compositions. Differences in the results may stem from XPS being a surface composition scan compared to EDX which can probe deeper within the drop-casted film. In the EDX measurement, there is a large sulfur signal which may indicate that the large presence of sulfur within the flakes meanwhile the XPS results show that a large amount of sulfur has been removed from the surface of the flakes and have been replaced by carbon, oxygen and nitrogen atoms from the solvent and atmosphere. This suggests that the carburization process begins from the surface of the flakes and aggregates and propagates from exterior to interior. In addition, the SEM results from Figure 5.5 shows that the carburization process does not affect the morphology of the material. This suggests that at lower femtosecond laser powers, the morphology of the material is marginally affected whilst still being able to carburize the material.

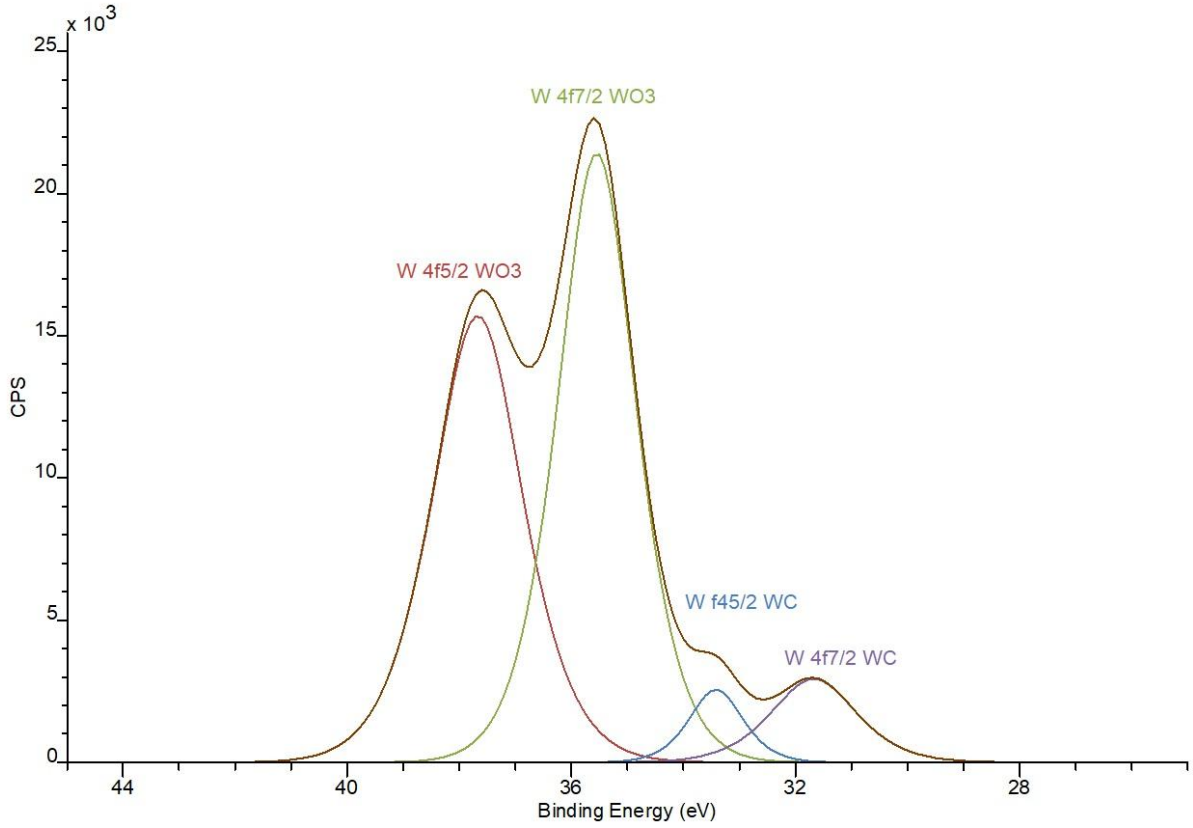

Figure 5.8 XPS scan of tungsten 4f spectra.

Continuing the XPS analysis, Figure 5.8 shows a detailed scan of the tungsten 4f spectra which reveal the bonds associated with tungsten. After deconvoluting the spectra, four prominent peaks are observed at 37.67, 35.55, 33.42 and 31.67 eV. The two peaks at 37.67 and 35.55 eV correspond to tungsten oxide or (WO_3) peaks from the 4f5/2 and 4f7/2 photoelectron lines respectively [71],[72]. Conversely, the other two peaks at 33.42 and 31.67 eV correspond to tungsten carbide bonds attributed to the W^{2+} ions which exist in both forms of tungsten carbide which are W_2C and WC [73]. The WO_3 peaks are larger, indicating there is a greater amount of oxidation on the surface which was also reported by Zhang et al. and attributed to the inevitable

surface oxidation in air [73]. Notably, no peaks corresponding to tungsten-sulfur bonds were observed.

Thus it can be concluded from the GIXRD data that the main crystallite structure consists of tungsten semi-carbide. The carburization process is caused by the femtosecond laser which begins at the surface of the nanoflakes as shown by the XPS surface composition. As the femtosecond laser power increases, the carburization continues to propagate deeper into the material as shown in the EDX results. In addition, EDX results show that functional groups containing oxygen at the surface of the material are removed as the femtosecond laser power increases. Sulfur compounds are found within the material shown by EDX; however as the femtosecond laser power increases, the sulfur is replaced by carbon, oxygen and nitrogen.

5.2.5 Raman Spectra

Raman spectroscopy was performed on both femtosecond laser irradiated WS_2 dissolved in acetonitrile and non-irradiated raw WS_2 powder. The femtosecond laser treatment of 0.4 W for 40 minutes was again used. Similar to previous characterization techniques, the femtosecond laser irradiated WS_2 was drop-casted onto a silicon wafer before analyzing. It was thought that the drop casting technique in atmospheric conditions might cause further oxidation of the femtosecond laser irradiated WS_2, thus the same femtosecond laser irradiated WS_2 was also drop-cast in a nitrogen-filled glovebox. Figure 5.9 shows the Raman spectra for the femtosecond laser irradiated WS_2 dropcasted in air and in a glovebox, in addition to the original non-irradiated WS_2 powder.

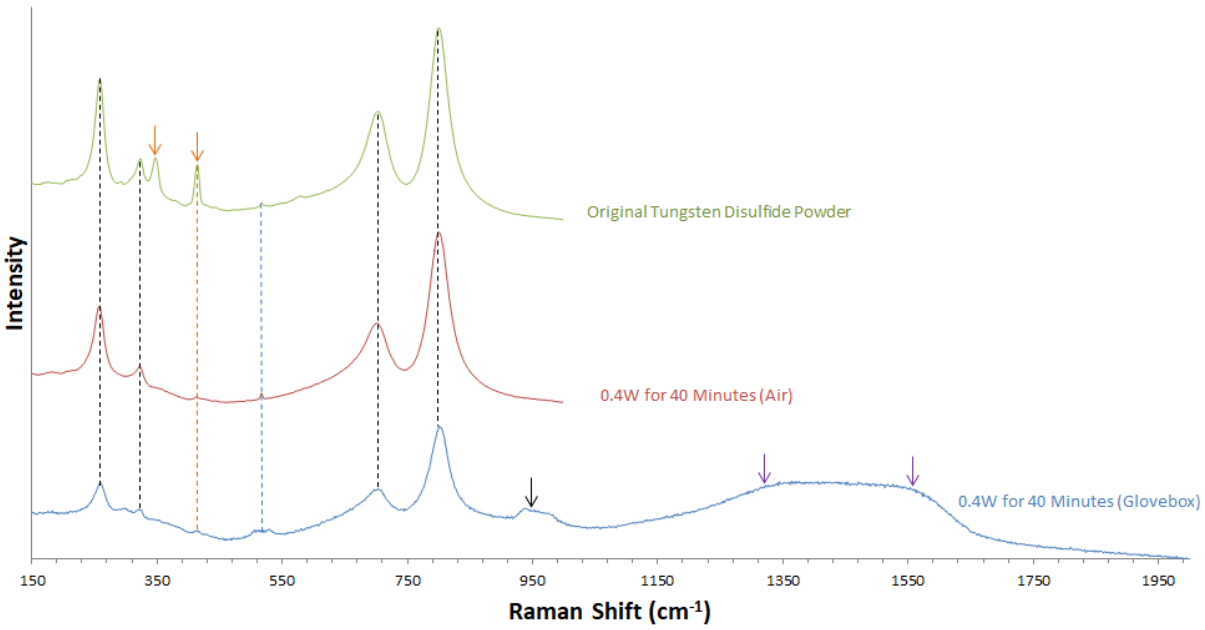

Figure 5.9 Raman spectra of non-irradiated WS_2 (green), femtosecond laser-carburized W_2C at 0.4W for 40 minutes drop-casted in air (red) and femtosecond laser-carburized W_2C at 0.4W for 40 minute drop-casted in glovebox (blue). Black dash lines and arrows belong to WO_3 bending and stretching modes. Orange dash lines and arrows belong to WS_2 vibrational modes. Purple arrows belong to the D and G peaks of carbon. Blue dashed line corresponds to a silicon oxide peak.

There are four peaks highlighted by the black dashed lines which correspond to tungsten oxide (WO_3) peaks. The two peaks centered around 260 and 320 cm^{-1} are attributed to the bending vibrations of O-W-O [74]. The other two WO_3 peaks centered around 700 and 800 cm^{-1} are attributed to the stretching modes of O-W-O [75]. Another broad peak highlighted by the black arrow at ~950 cm^{-1} may correspond to the W=O stretching mode [75]. Moreover, another two peaks highlighted by the orange arrows correspond to tungsten disulfide (WS_2) peaks. From literature, these two peaks centered at around 345 and 415 cm^{-1} correspond to the in-plane vibrational E^1_{2g} mode and the out-of-plane vibrational A_{1g} mode [76]. There is a very small peak centered around 515 cm^{-1} which corresponds to the unwanted but observed Si-O bonds which can be attributed to the silicon wafer used for drop casting [77]. The last two characteristic peaks highlighted by the purple arrows centered around 1350 and 1585 cm^{-1} correspond to the D and G

peaks of amorphous carbon [78]. These carbon peaks agree with GIXRD characterization which indicates that there is a high degree of carburization after using the femtosecond laser to irradiate the WS_2. Interestingly, the four peaks highlighted in the black dashed lines may instead correspond to tungsten carbide W-C bonds rather than WO_3 according to Yan et al. where the Raman peaks of W-C bonds were centered around 266, 326, 709 and 806 cm^{-1} [79]. In this way it is difficult to rely solely on Raman spectra as both WO_3 and W-C bond peaks may overlap.

It is evident from the Raman spectra that using the femtosecond laser to irradiate the WS_2 powder dissolved in acetonitrile has an effect on the chemical composition. For example, the two peaks highlighted by the orange arrows which correspond to vibrational modes of WS_2 are almost completely gone in the samples that were femtosecond laser treated. This indicates that much of the sulfur from the original WS_2 has been replaced by either oxygen or carbon, consistent with the XPS results in Table 5.5. Also, the presence of the D & G carbon peaks found on the laser-treated WS_2 samples appear to be consistent with the carburization of WS_2.

Moreover, the original WS_2 powder contains strong WO_3 peaks, in agreement with the GIXRD and EDX data which show that some of the WS_2 powder had already been oxidized before the femtosecond laser irradiation. As for the effects of drop-casting in a nitrogen-filled glovebox, it appears that there may be a slight influence on the amount of oxidation found in the Raman spectra. More specifically, WO_3 peaks highlighted with the dashed black lines are less prominent in the femtosecond laser irradiated sample which was drop-casted in a nitrogen glove box instead of air.

Overall, the Raman spectra show that the original WS_2 starting material is not pure and contains WO_3 which can be attributed to natural oxidation in air. In addition, using the femtosecond laser to irradiate the WS_2 dissolved in acetonitrile changes the chemical composition of the material via substituting the sulfur atoms with both carbon and oxygen. The main source of carbon comes from the breakdown of acetonitrile via the femtosecond laser which replaces the sulfur atoms creating W_2C, although the presence of W_2C is difficult to observe by Raman spectroscopy due to overlap with WO_3 peaks.

5.3 Optical Properties of 2D Tungsten Semi-carbide

Exploring the optical properties of the 2D tungsten semi-carbide can assist in determining the effects of the femtosecond laser irradiation on WS_2 dissolved in acetonitrile. In addition, understanding the absorbance can give insight on the photothermal properties of the newly synthesized material. More specifically, the absorbance spectra will determine the amount of energy being absorbed at various wavelengths of light with some light being reflected or scattered. The currently understood photothermal mechanism for tungsten semi-carbide stems from electron-hole pair generation via interband transitions [81]. As light is absorbed in the NIR range, electron-hole pairs are generated within the metallic W_2C which create heat as the pairs recombine.

5.3.1 Absorbance

Figure 5.10 shows absorbance measurements of WS_2 dissolved in acetonitrile irradiated with various laser parameters (0.2W for 20 minutes, 0.4W for 40 minutes, 0.8W for 40 minutes, 1W for 45 minutes, 2W for 45 minutes and 4W for 45 minutes). The absorbance spectra is found to

be consistent with Li et al., which describes a broad flat absorbance spectra for W_2C in the NIR range [81].

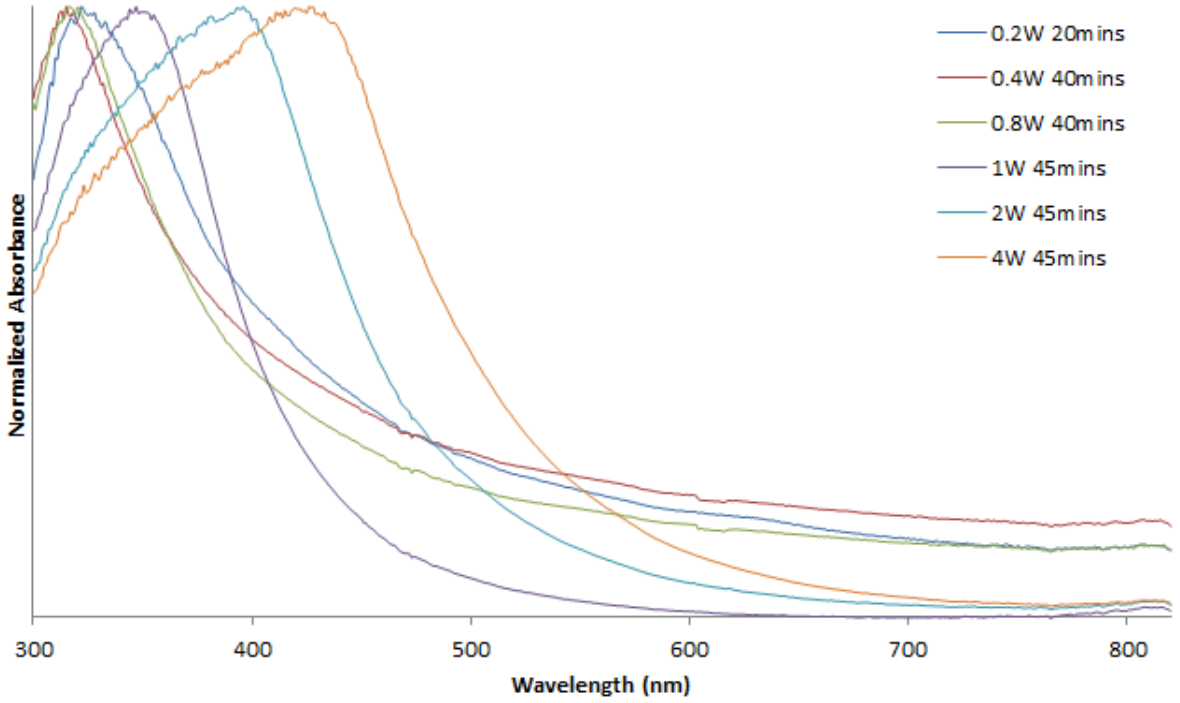

Figure 5.10 Absorbance spectra of femtosecond irradiated WS_2 with varying laser powers (0.2, 0.4, 0.8, 1, 2 and 4 W).

The normalized absorbance spectra shown in Figure 5.10 show an obvious peak shift as the femtosecond laser power increases. This effect seems to be most prevalent as the femtosecond laser power increases above 1 W. From literature, polar solvents are known to redshift (bathochromic shift) as the polarity is changed due to the decrease in energy gap of the solvent molecules [80]. As the polarity of the solvent decreases, the absorbance spectra tends to redshift due to the formation of hydrogen bonds between the solvent molecules and the nanoparticles. As the solvent polarity changes, the absorption of the nanoparticles also changes. This agrees with the carburization of WS_2 as W_2C has a much lower energy gap in comparison to WS_2. Here the

femtosecond laser is expected to break down the acetonitrile which is a polar solvent, causing the polarity to change. This may allow new hydrogen bonds to form between the nanosheets and the modified solvent, which ultimately causes a redshift in the absorbance. This is demonstrated as there is a clear redshift corresponding to the increase in laser power.

Table 5.6 Absorbance values at 808 nm of femtosecond laser-treated WS_2 in acetonitrile with different femtosecond laser settings

Femtosecond Laser Parameter	**Absorbance Value at 808 nm**
0.2 W for 20 Minutes	0.213
0.4 W for 40 Minutes	0.295
0.8 W for 40 Minutes	0.207
1 W for 45 Minutes	0.029
2 W for 45 Minutes	0.062
4 W for 45 Minutes	0.079

Another interesting trend in the absorbance spectra is the broad absorbance of the femtosecond laser-treated WS_2 samples with lower laser powers between 0.2 to 0.8 W. The absorbance of these samples extends into the NIR-I range. However this is not the case when higher femtosecond laser powers (between 1 to 4 W) are used which result in poor absorption in the NIR region as seen in Table 5.6 describing the absorbance at 808 nm. More material characterization of the higher femtosecond laser power WS_2 materials is needed to explain the differences in absorption.

Currently the best NIR-I absorbent femtosecond laser treated material uses 0.4W at 40 minutes as seen in Table 5.6. However, there may be a more optimal set of femtosecond laser parameters

which allow for better NIR-I absorbance. Overall, the femtosecond laser irradiated WS_2 samples with high NIR-I absorbances are promising candidates for photothermal therapy.

5.4 Photothermal Properties of Two Dimensional Tungsten Carbide

Photothermal conversion efficiencies of WS_2 samples irradiated in acetonitrile were measured via the method described in Chapter 3. A series of 12 femtosecond laser-treated samples with varying laser powers and irradiation times were measured to compare the effects of femtosecond laser irradiation on the PTCE. Table 5.6 shows the PTCE values, along with the energy imparted by the laser treatment, absorbance, temperature change, and time constant. In comparison to the non-irradiated WS_2 samples, there is a significant improvement in the PTCE for some irradiated samples.

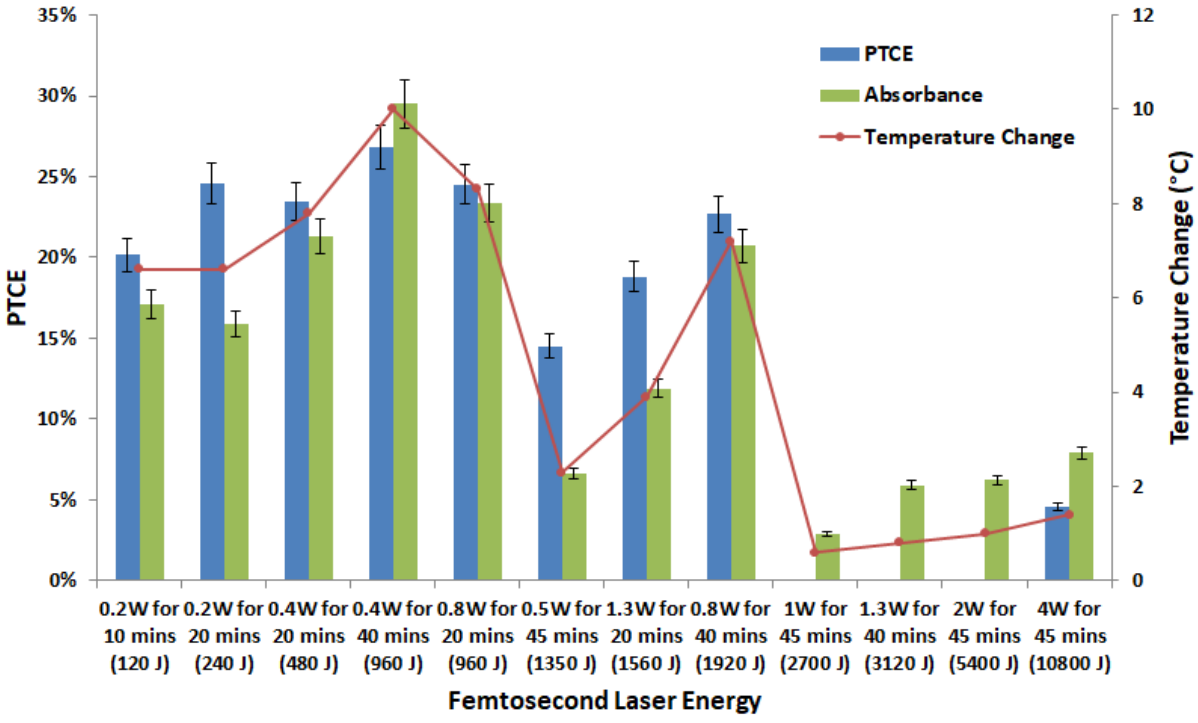

Figure 5.11 PTCE, absorbance and temperature change values of femtosecond irradiated WS_2 at varying laser powers and irradiation times.

From the results shown in Table 5.11, it appears that lower-energy femtosecond laser treatments result in relatively high PTCE values above 20%. The temperature change and absorbance also follows this trend and reach a maximum at around 960 J of irradiation energy, corresponding to a femtosecond laser power of 0.4W and irradiation for 40 minutes.

Typically, using low-powered femtosecond irradiation resulted in a dark grey solution, however as the femtosecond laser power increased the solution turned yellow, then orange, then red, with each increment of power. This is shown in Figure 5.12 in which the color of the nanoparticle solution changes as the femtosecond laser power increases from 0.5W, 1W, 2W and finally 4W.

Figure 5.12 Solution color changes of femtosecond irradiated WS_2 with varying laser powers (0.5, 1, 2, 4W for 45 minutes).

Currently, material characterization has not been performed on the higher femtosecond laser power samples, since the PTCE values were low. It is suspected that the original WS_2 material has undergone drastic changes to undergo such color changes. This requires more characterization on the higher femtosecond laser-treated WS_2 samples to determine the cause of the changes.

Chapter 6 Conclusions and Future Work

A femtosecond laser is used to alter the morphology, stoichiometry and chemistry of both tungsten disulfide and molybdenum disulfide powders as starting materials. Through material characterization, novel synthesis methods for creating two dimensional tungsten semi-carbide through carburizing tungsten disulfide and synthesizing plasmonic substoichiometric molybdenum oxide through the partial oxidation of molybdenum disulfide are found.

Optical and photothermal studies were conducted to determine the feasibility of these materials as a photothermal agent used in photothermal therapy. Absorption spectroscopy was used to study the materials' interaction with light, specifically in the near infrared (NIR) wavelengths. A custom measurement system was designed and engineered to measure the PTCE. The highest PTCE was measured to be 27% and 33% for W_2C and MoO_{3-x} respectively. This suggests both materials are strong candidates as a photothermal agent for use in photothermal therapy. Currently there is still more research to be done in regards to improving the accuracy of the PTCE measurements. Using an infrared camera instead of a thermocouple probe may be more advantageous as non-contact temperature measurements prevent cross-contamination between experiments as thermocouple probes have to be cleaned after each sample. In addition, the absorbance measurements should ideally be performed on a UV-Vis spectrometer for optimal accuracy instead of the spectrofluorometer. Furthermore, the 3D printed cuvette holder can be redesigned to secure the laser better in addition to being able to swap out between different lasers. Currently the laser is pressed into the 3D printed holder which is not a great long term solution for durability. However, the current PTCE system is still more than capable of determining the PTCE of any nanomaterials dissolved in solution. In the future it may be possible to modify the system to measure solid samples by measuring the temperature change

via a non-contact infrared camera. In addition the integration of a 1064 nm laser for measuring the PTCE of nanomaterials in the NIR-II range can be implemented in the future. Many studies have not explored the NIR-II photothermal responses of different nanomaterials and can be studied with the addition of the 1064 nm laser.

The plasmonic substoichiometric molybdenum oxide nanomaterials still have much to research as tuning the laser treatment time, power and ethanol concentration to obtain a higher PTCE is still needed. Currently the highest PTCE values (~40%) are achieved with MoS_2 dissolved in a 95% ethanol solution converted to MoO_{3-x} by being laser-treated at 2W for 25 minutes. However, different synthesis methods are currently being explored such as directly using a mixture of molybdenum oxide (MoO_3) and molybdenum metal (Mo) as the starting powder before femtosecond laser treatment. This method has resulted in promisingly high PTCEs in the range of ~40% which may be better than using MoS_2 as the starting material. Similarly, another novel method without using the femtosecond laser has been researched which includes using a heated ultrasonic bath to synthesize MO_{3-x} from MoO_3 as the starting material. This method can achieve PTCE values of up to ~38% which is promising as only pure water is involved in the synthesis process. This removes the requirement of freeze-drying and redispursing the nanoparticles in water for biological applications.

Similarly, the two dimensional tungsten semi-carbide derived from tungsten disulfide also has more opportunities for improvement and insight. For instance it is still not entirely clear the effects of increasing the femtosecond laser power. The PTCE in the NIR range may significantly decrease; however, more material characterization must be done to understand effects on the

size, morphology and chemistry of the material. In addition, tuning the amount of carburization and oxidation by using different solvents or femtosecond laser parameters is key to understanding the photothermal behaviour of the material. Tungsten semi-carbide itself is an interesting material that is not common in photothermal therapy research. Currently only the NIR-II photothermal properties [84] have been explored, which leaves room for much to experiment and discover. The best PTCE values from the W_2C material is ~26% which is quite average and can be improved by understanding and tuning the material properties via the femtosecond laser.

Future work could include exploring the NIR-II photothermal conversion properties of nanomaterials and designing a PTCE measurement system to do in-vitro PTCE measurements. The NIR-II range sparks great research interest as it is able to penetrate deeper into tissue and reach deep tumors in contrast to NIR-I which would require higher laser powers to reach the same depths as NIR-II lasers [85]. In addition, designing an in-vitro PTCE measurement system would allow for in-vitro photothermal therapy tests which further advances the understanding of photothermal therapy. Possible setups would include using well plates that contain cell tissues injected with photothermal agents which are measured via a non-contact infrared camera. The NIR laser would be situated above the well plates to maximize irradiation while the infrared camera is situated offset by the NIR laser in order to measure temperature without interference from the NIR laser.

Overall, there are many areas of research that may arise from this work such as nanomaterial synthesis, material characterization, PTCE system design and in-vitro photothermal testing.

Cancer, although an intimidating prognosis, is becoming a more treatable disease with advancements in photothermal therapy research which creates progress for the betterment of human life.

Bibliography

[1] K. Sikora and K. E. Halnan, *Treatment of cancer*. Boca Raton, Florida: London Chapman and Hall, 1990.

[2] J. Jankowski and J. Franklin, "Faculty Opinions recommendation of Global cancer statistics 2018: GLOBOCAN estimates of incidence and mortality worldwide for 36 cancers in 185 countries.," *Faculty Opinions – Post-Publication Peer Review of the Biomedical Literature*, 2020.

[3] J. van der Zee, "Heating the patient: a promising approach?," *Annals of Oncology*, vol. 13, no. 8, pp. 1173–1184, 2002.

[4] X. Huang, I. H. El-Sayed, W. Qian, and M. A. El-Sayed, "Cancer Cell Imaging and Photothermal Therapy in the Near-Infrared Region by Using Gold Nanorods," *Journal of the American Chemical Society*, vol. 128, no. 6, pp. 2115–2120, 2006.

[5] D. de Melo-Diogo, C. Pais-Silva, D. R. Dias, A. F. Moreira, and I. J. Correia, "Strategies to Improve Cancer Photothermal Therapy Mediated by Nanomaterials," Advanced Healthcare Materials, vol. 6, no. 10, p. 1700073, 2017.

[6] S. He, J. Song, J. Qu, and Z. Cheng, "Crucial breakthrough of second near-infrared biological window fluorophores: design and synthesis toward multimodal imaging and theranostics," Chemical Society Reviews, vol. 47, no. 12, pp. 4258–4278, 2018.

[7] C. Zhou, M. Long, Y. Qin, X. Sun, and J. Zheng, "Luminescent Gold Nanoparticles with Efficient Renal Clearance," Angewandte Chemie, vol. 123, no. 14, pp. 3226–3230, 2011.

[8] E. Blanco, H. Shen, and M. Ferrari, "Principles of Nanoparticle Design for Overcoming Biological Barriers to Drug Delivery *," *Nanomaterials and Neoplasms*, pp. 585–622, 2021.

[9] S. Wang, K. Li, Y. Chen, H. Chen, M. Ma, J. Feng, Q. Zhao, and J. Shi, “Biocompatible PEGylated MoS2 nanosheets: Controllable bottom-up synthesis and highly efficient photothermal regression of tumor,” Biomaterials, vol. 39, pp. 206–217, 2015.

[10] S. Tang, X. Huang, and N. Zheng, “Silica coating improves the efficacy of Pd nanosheets for photothermal therapy of cancer cells using near infrared laser,” Chemical Communications, vol. 47, no. 13, p. 3948, 2011.

[11] K. Yang, S. Zhang, G. Zhang, X. Sun, S.-T. Lee, and Z. Liu, “Graphene in Mice: Ultrahigh In Vivo Tumor Uptake and Efficient Photothermal Therapy,” Nano Letters, vol. 10, no. 9, pp. 3318–3323, 2010.

[12] Z. Liu, J. T. Robinson, X. Sun, and H. Dai, “PEGylated Nanographene Oxide for Delivery of Water-Insoluble Cancer Drugs,” Journal of the American Chemical Society, vol. 130, no. 33, pp. 10876–10877, 2008.

[13] H. Bao, Y. Pan, Y. Ping, N. G. Sahoo, T. Wu, L. Li, J. Li, and L. H. Gan, “Chitosan-Functionalized Graphene Oxide as a Nanocarrier for Drug and Gene Delivery,” Small, vol. 7, no. 11, pp. 1569–1578, 2011.

[14] O. A. Savchuk, J. J. Carvajal, J. Massons, M. Aguiló, and F. Díaz, “Determination of photothermal conversion efficiency of graphene and graphene oxide through an integrating sphere method,” Carbon, vol. 103, pp. 134–141, 2016.

[15] D. Pasquier and O. V. Yazyev, “Crystal field, ligand field, and interorbital effects in two-dimensional transition metal dichalcogenides across the periodic table,” 2D Materials, vol. 6, no. 2, p. 025015, 2019.

[16] H. Yi, X. Zhou, C. Zhou, Q. Yang, and N. Jia, “Liquid exfoliated biocompatible WS2@BSA nanosheets with enhanced theranostic capacity,” Biomaterials Science, vol. 9, no. 1, pp. 148–156, 2021.

[17] X.-Z. Cui, Z.-G. Zhou, Y. Yang, J. Wei, J. Wang, M.-W. Wang, H. Yang, Y.-J. Zhang, and S.-P. Yang, “PEGylated WS2 nanosheets for X-ray computed tomography imaging and photothermal therapy,” Chinese Chemical Letters, vol. 26, no. 6, pp. 749–754, 2015.

[18] Y. Yong, X. Cheng, T. Bao, M. Zu, L. Yan, W. Yin, C. Ge, D. Wang, Z. Gu, and Y. Zhao, “Tungsten Sulfide Quantum Dots as Multifunctional Nanotheranostics for In Vivo Dual-Modal Image-Guided Photothermal/Radiotherapy Synergistic Therapy,” ACS Nano, vol. 9, no. 12, pp. 12451–12463, 2015.

[19] W. Yin, L. Yan, J. Yu, G. Tian, L. Zhou, X. Zheng, X. Zhang, Y. Yong, J. Li, Z. Gu, and Y. Zhao, “High-Throughput Synthesis of Single-Layer MoS2 Nanosheets as a Near-Infrared Photothermal-Triggered Drug Delivery for Effective Cancer Therapy,” ACS Nano, vol. 8, no. 7, pp. 6922–6933, 2014.

[20] W. Feng, L. Chen, M. Qin, X. Zhou, Q. Zhang, Y. Miao, K. Qiu, Y. Zhang, and C. He, “Flower-like PEGylated MoS2 nanoflakes for near-infrared photothermal cancer therapy,” Scientific Reports, vol. 5, no. 1, 2015.

[21] X. Zhang, J. Wu, G. R. Williams, S. Niu, Q. Qian, and L.-M. Zhu, “Functionalized MoS2-nanosheets for targeted drug delivery and chemo-photothermal therapy,” Colloids and Surfaces B: Biointerfaces, vol. 173, pp. 101–108, 2019.

[22] B. Anasori and Y. Gogotsi, “Introduction to 2D Transition Metal Carbides and Nitrides (MXenes),” 2D Metal Carbides and Nitrides (MXenes), pp. 3–12, 2019.

[23] K. Maleski, C. E. Ren, M.-Q. Zhao, B. Anasori, and Y. Gogotsi, “Size-Dependent Physical and Electrochemical Properties of Two-Dimensional MXene Flakes,” ACS Applied Materials & Interfaces, vol. 10, no. 29, pp. 24491–24498, 2018.

[24] Y. Qiu, “Two-Dimensional Materials Beyond Graphene: Emerging Opportunities for Biomedicine,” Nano LIFE, vol. 06, no. 03n04, p. 1642008, 2016.

[25] H. Lin, X. Wang, L. Yu, Y. Chen, and J. Shi, “Two-Dimensional Ultrathin MXene Ceramic Nanosheets for Photothermal Conversion,” Nano Letters, vol. 17, no. 1, pp. 384–391, 2016.

[26] H. Lin, S. Gao, C. Dai, Y. Chen, and J. Shi, “A Two-Dimensional Biodegradable Niobium Carbide (MXene) for Photothermal Tumor Eradication in NIR-I and NIR-II Biowindows,” Journal of the American Chemical Society, vol. 139, no. 45, pp. 16235–16247, 2017.

[27] H. Lin, Y. Wang, S. Gao, Y. Chen, and J. Shi, “Theranostic 2D Tantalum Carbide (MXene),” Advanced Materials, vol. 32, no. 42, p. 2003085, 2020.

[28] K. Huang, Z. Li, J. Lin, G. Han, and P. Huang, “Two-dimensional transition metal carbides and nitrides (MXenes) for biomedical applications,” Chemical Society Reviews, vol. 47, no. 17, pp. 6889–6889, 2018.

[29] X. Wang and L. Cheng, “Multifunctional two-dimensional nanocomposites for photothermal-based combined cancer therapy,” Nanoscale, vol. 11, no. 34, pp. 15685–15708, 2019.

[30] D.-K. Ji, C. Ménard-Moyon, and A. Bianco, “Physically-triggered nanosystems based on two-dimensional materials for cancer theranostics,” Advanced Drug Delivery Reviews, vol. 138, pp. 211–232, 2019.

[31] A. H. Castro Neto and et al. et al., “Strong Light-Matter Interactions in Heterostructures of Atomically Thin Films.,” ChemInform, vol. 44, no. 37, 2013.

[32] M. Ye, D. Winslow, D. Zhang, R. Pandey, and Y. Yap, “Recent Advancement on the Optical Properties of Two-Dimensional Molybdenum Disulfide (MoS2) Thin Films,” Photonics, vol. 2, no. 1, pp. 288–307, 2015.

[33] J. Chen, C. Liu, D. Hu, F. Wang, H. Wu, X. Gong, X. Liu, L. Song, Z. Sheng, and H. Zheng, “Single-Layer MoS2 Nanosheets with Amplified Photoacoustic Effect for Highly Sensitive Photoacoustic Imaging of Orthotopic Brain Tumors,” Advanced Functional Materials, vol. 26, no. 47, pp. 8715–8725, 2016.

[34] G. Yang, R. Zhang, C. Liang, H. Zhao, X. Yi, S. Shen, K. Yang, L. Cheng, and Z. Liu, “Manganese Dioxide Coated WS2@Fe3O4/s SiO2 Nanocomposites for pH-Responsive MR Imaging and Oxygen-Elevated Synergetic Therapy,” Small, vol. 14, no. 2, p. 1702664, 2017.

[35] J. Xuan, Z. Wang, Y. Chen, D. Liang, L. Cheng, X. Yang, Z. Liu, R. Ma, T. Sasaki, and F. Geng, “Organic-Base-Driven Intercalation and Delamination for the Production of Functionalized Titanium Carbide Nanosheets with Superior Photothermal Therapeutic Performance,” Angewandte Chemie International Edition, vol. 55, no. 47, pp. 14569–14574, 2016.

[36] H. Yin, Y. Kuwahara, K. Mori, H. Cheng, M. Wen, Y. Huo, and H. Yamashita, “Localized Surface Plasmon Resonances in Plasmonic Molybdenum Tungsten Oxide Hybrid for Visible-Light-Enhanced Catalytic Reaction,” The Journal of Physical Chemistry C, vol. 121, no. 42, pp. 23531–23540, 2017.

[37] M. L. Brongersma, N. J. Halas, and P. Nordlander, “Plasmon-induced hot carrier science and technology,” Nature Nanotechnology, vol. 10, no. 1, pp. 25–34, 2015.

[38] J. A. Webb and R. Bardhan, “Emerging advances in nanomedicine with engineered gold nanostructures,” Nanoscale, vol. 6, no. 5, p. 2502, 2014.

[39] S. Sarina, E. R. Waclawik, and H. Zhu, “ChemInform Abstract: Photocatalysis on Supported Gold and Silver Nanoparticles under Ultraviolet and Visible Light Irradiation,” ChemInform, vol. 44, no. 38, 2013.

[40] C. M. Hessel, V. P. Pattani, M. Rasch, M. G. Panthani, B. Koo, J. W. Tunnell, and B. A. Korgel, “Copper Selenide Nanocrystals for Photothermal Therapy,” Nano Letters, vol. 11, no. 6, pp. 2560–2566, 2011.

[41] J. Wang, Y. Li, L. Deng, N. Wei, Y. Weng, S. Dong, D. Qi, J. Qiu, X. Chen, and T. Wu, “High-Performance Photothermal Conversion of Narrow-Bandgap Ti2O3Nanoparticles,” Advanced Materials, vol. 29, no. 3, p. 1603730, 2016.

[42] Z. Xie, Y. Duo, Z. Lin, T. Fan, C. Xing, L. Yu, R. Wang, M. Qiu, Y. Zhang, Y. Zhao, X. Yan, and H. Zhang, “The Rise of 2D Photothermal Materials beyond Graphene for Clean Water Production,” Advanced Science, vol. 7, no. 5, p. 1902236, 2020.

[43] C. Chen, Y. Kuang, and L. Hu, “Challenges and Opportunities for Solar Evaporation,” Joule, vol. 3, no. 3, pp. 683–718, 2019.

[44] J. R. Vélez-Cordero and J. Hernández-Cordero, “Heat generation and conduction in PDMS-carbon nanoparticle membranes irradiated with optical fibers,” International Journal of Thermal Sciences, vol. 96, pp. 12–22, 2015.

[45] K. Ibrahim, I. Novodchuk, K. Mistry, M. Singh, C. Ling, J. Sanderson, M. Bajcsy, M. Yavuz, and K. P. Musselman, “Laser‐Directed Assembly of Nanorods of 2D Materials,” Small, vol. 15, no. 46, p. 1904415, 2019.

[46] K. H. Ibrahim, M. Irannejad, B. Wales, J. Sanderson, M. Yavuz, and K. P. Musselman, “Simultaneous Fabrication and Functionalization of Nanoparticles of 2D Materials with Hybrid Optical Properties,” Advanced Optical Materials, vol. 6, no. 11, p. 1701365, 2018.

[47] F. Ye, D. Chang, A. Ayub, K. Ibrahim, A. Shahin, R. Karimi, S. Wettig, J. Sanderson, and K. P. Musselman, “Synthesis of Two-Dimensional Plasmonic Molybdenum Oxide Nanomaterials by Femtosecond Laser Irradiation,” Chemistry of Materials, 2021.

[48] D. K. Roper, W. Ahn, and M. Hoepfner, “Microscale Heat Transfer Transduced by Surface Plasmon Resonant Gold Nanoparticles,” The Journal of Physical Chemistry C, vol. 111, no. 9, pp. 3636–3641, 2007.

[49] E. Ataş Berksoy, Ö. Bağ, S. Yazici, and T. Çelik, “Use of noncontact infrared thermography to measure temperature in children in a triage room,” Medicine, vol. 97, no. 5, 2018.

[50] A. J. Bach, I. B. Stewart, A. E. Disher, and J. T. Costello, “A Comparison between Conductive and Infrared Devices for Measuring Mean Skin Temperature at Rest, during Exercise in the Heat, and Recovery,” PLOS ONE, vol. 10, no. 2, 2015.

[51] N. Neumann and V. Banta, “P12 - Comparison of Pyroelectric and Thermopile Detectors,” Proceedings IRS² 2013, 2013.

[52] K. F. Mak, C. Lee, J. Hone, J. Shan, and T. F. Heinz, “Atomically Thin MoS2: A New Direct-Gap Semiconductor,” Physical Review Letters, vol. 105, no. 13, 2010.

[53] A. Splendiani, L. Sun, Y. Zhang, T. Li, J. Kim, C.-Y. Chim, G. Galli, and F. Wang, “Emerging Photoluminescence in Monolayer MoS2,” Nano Letters, vol. 10, no. 4, pp. 1271–1275, 2010.

[54] W. Zhao, Z. Ghorannevis, L. Chu, M. Toh, C. Kloc, P.-H. Tan, and G. Eda, “Evolution of Electronic Structure in Atomically Thin Sheets of WS2 and WSe2,” ACS Nano, vol. 7, no. 1, pp. 791–797, 2012.

[55] C. Dai, H. Lin, G. Xu, Z. Liu, R. Wu, and Y. Chen, “Biocompatible 2D Titanium Carbide (MXenes) Composite Nanosheets for pH-Responsive MRI-Guided Tumor Hyperthermia,” Chemistry of Materials, vol. 29, no. 20, pp. 8637–8652, 2017.

[56] H. Lin, X. Wang, L. Yu, Y. Chen, and J. Shi, “Two-Dimensional Ultrathin MXene Ceramic Nanosheets for Photothermal Conversion,” Nano Letters, vol. 17, no. 1, pp. 384–391, 2016.

[57] Z. Liu, M. Zhao, H. Lin, C. Dai, C. Ren, S. Zhang, W. Peng, and Y. Chen, “2D magnetic titanium carbide MXene for cancer theranostics,” Journal of Materials Chemistry B, vol. 6, no. 21, pp. 3541–3548, 2018.

[58] Y. Gao, W. Huang, C. Yang, Z. Liu, H. Meng, B. Yang, Y. Xu, and C. Guo, “Targeted photothermal therapy of mice and rabbits realized by macrophage-loaded tungsten carbide,” *Biomaterials Science*, vol. 7, no. 12, pp. 5350–5358, 2019.

[59] M. M. Alsaif, M. R. Field, T. Daeneke, A. F. Chrimes, W. Zhang, B. J. Carey, K. J. Berean, S. Walia, J. van Embden, B. Zhang, K. Latham, K. Kalantar-zadeh, and J. Z. Ou, “Exfoliation Solvent Dependent Plasmon Resonances in Two-Dimensional Sub-Stoichiometric Molybdenum Oxide Nanoflakes,” ACS Applied Materials & Interfaces, vol. 8, no. 5, pp. 3482–3493, 2016.

[60] M. M. Alsaif, A. F. Chrimes, T. Daeneke, S. Balendhran, D. O. Bellisario, Y. Son, M. R. Field, W. Zhang, H. Nili, E. P. Nguyen, K. Latham, J. van Embden, M. S. Strano, J. Z. Ou, and K. Kalantar-zadeh, “High-Performance Field Effect Transistors Using Electronic Inks of 2D Molybdenum Oxide Nanoflakes,” Advanced Functional Materials, vol. 26, no. 1, pp. 91–100, 2015.

[61] K. Manthiram and A. P. Alivisatos, “Tunable Localized Surface Plasmon Resonances in Tungsten Oxide Nanocrystals,” *Journal of the American Chemical Society*, vol. 134, no. 9, pp. 3995–3998, 2012.

[62] M. Mohsen-Nia, H. Amiri, and B. Jazi, “Dielectric Constants of Water, Methanol, Ethanol, Butanol and Acetone: Measurement and Computational Study,” Journal of Solution Chemistry, vol. 39, no. 5, pp. 701–708, 2010.

[63] T. Leelawattananon and S. Chittayasothorn, “Simulation Effects on the Optical Response of Gold Nanoparticles,” Proceedings of the 9th International Conference on Simulation and Modeling Methodologies, Technologies and Applications, 2019.

[64] M. M. Alsaif, K. Latham, M. R. Field, D. D. Yao, N. V. Medhekar, G. A. Beane, R. B. Kaner, S. P. Russo, J. Z. Ou, and K. Kalantar-zadeh, “Tunable Plasmon Resonances in Two-Dimensional Molybdenum Oxide Nanoflakes,” Advanced Materials, vol. 26, no. 29, pp. 4919–4919, 2014.

[65] L. Zheng, Y. Xu, D. Jin, and Y. Xie, “Novel Metastable Hexagonal MoO3 Nanobelts: Synthesis, Photochromic, and Electrochromic Properties,” Chemistry of Materials, vol. 21, no. 23, pp. 5681–5690, 2009.

[66] S. Adams, “CDW Superstructures in Hydrogen Molybdenum Bronzes HxMoO3,” *Journal of Solid State Chemistry*, vol. 149, no. 1, pp. 75–87, 2000.

[67] A. S. Kurlov and A. I. Gusev, Tungsten carbides: structure, properties and application in hardmetals. Cham, Zug: Springer, 2016.

[68] Y. Hara, N. Minami, and H. Itagaki, “Synthesis and characterization of high-surface area tungsten carbides and application to electrocatalytic hydrogen oxidation,” *Applied Catalysis A: General*, vol. 323, pp. 86–93, 2007.

[69] Y. Hara, N. Minami, H. Matsumoto, and H. Itagaki, “A Novel Preparation of Tungsten Carbide Particles with High Specific Surface Area by Carburizing Tungsten Sulfides,” Chemistry Letters, vol. 36, no. 2, pp. 286–287, 2007.

[70] A. Sevy, R. F. Huffaker, and M. D. Morse, “Bond Dissociation Energies of Tungsten Molecules: WC, WSi, WS, WSe, and WCl,” The Journal of Physical Chemistry A, vol. 121, no. 49, pp. 9446–9457, 2017.

[71] T. H. Fleisch and G. J. Mains, “An XPS study of the UV reduction and photochromism of MoO3 and WO3,” The Journal of Chemical Physics, vol. 76, no. 2, pp. 780–786, 1982.

[72] S. F. Ho, S. Contarini, and J. W. Rabalais, “Ion-beam-induced chemical changes in the oxyanions (Moyn-) and oxides (Mox) where M = chromium, molybdenum, tungsten, vanadium, niobium and tantalum,” The Journal of Physical Chemistry, vol. 91, no. 18, pp. 4779–4788, 1987.

[73] L.-N. Zhang, Y.-Y. Ma, Z.-L. Lang, Y.-H. Wang, S. U. Khan, G. Yan, H.-Q. Tan, H.-Y. Zang, and Y.-guang Li, “Ultrafine cable-like WC/W2C heterojunction nanowires covered by graphitic carbon towards highly efficient electrocatalytic hydrogen evolution,” Journal of Materials Chemistry A, vol. 6, no. 31, pp. 15395–15403, 2018.

[74] A. Kromka, J. Janik, A. Satka, and J. Pavlov, “Investigation of carburisation of Tungsten-Carbide formation by hot-filament CVD technique,” Acta Physica Slovaca, vol. 51, no. 6, pp. 359–368, 2001.

[75] A. Rougier, F. Portemer, A. Quédé, and M. El Marssi, “Characterization of pulsed laser deposited WO3 thin films for electrochromic devices,” Applied Surface Science, vol. 153, no. 1, pp. 1–9, 1999.

[76] H. Zeng, G.-B. Liu, J. Dai, Y. Yan, B. Zhu, R. He, L. Xie, S. Xu, X. Chen, W. Yao, and X. Cui, “Optical signature of symmetry variations and spin-valley coupling in atomically thin tungsten dichalcogenides,” Scientific Reports, vol. 3, no. 1, 2013.

[77] F. S. Manciu, J. L. Enriquez, W. G. Durrer, Y. Yun, C. V. Ramana, and S. K. Gullapalli, “Spectroscopic analysis of tungsten oxide thin films,” Journal of Materials Research, vol. 25, no. 12, pp. 2401–2406, 2010.

[78] S. E. Mrabet, M. D. Abad, C. López-Cartes, D. Martínez-Martínez, and J. C. Sánchez-López, “Thermal Evolution of WC/C Nanostructured Coatings by Raman and In Situ XRD Analysis,” Plasma Processes and Polymers, vol. 6, no. S1, 2009.

[79] Y. Yan, B. Xia, X. Qi, H. Wang, R. Xu, J.-Y. Wang, H. Zhang, and X. Wang, “Nano-tungsten carbide decorated graphene as co-catalysts for enhanced hydrogen evolution on molybdenum disulfide,” Chemical Communications, vol. 49, no. 43, p. 4884, 2013.

[80] E. E. Tseplin, S. N. Tseplina, and O. G. Khvostenko, “Mechanisms of specific effects of polar solvent in optical absorption spectra,” Optics and Spectroscopy, vol. 110, no. 6, pp. 903–909, 2011.

[81] Y. L. Wang, T. Nie, Y. H. Li, X. L. Wang, L. R. Zheng, A. P. Chen, X. Q. Gong, and H. G. Yang, “Black Tungsten Nitride as a Metallic Photocatalyst for Overall Water Splitting Operable at up to 765 nm,” *Angewandte Chemie*, vol. 129, no. 26, pp. 7538–7542, 2017.

[82] K. K. Kam and B. A. Parkinson, “Detailed photocurrent spectroscopy of the semiconducting group VIB transition metal dichalcogenides,” The Journal of Physical Chemistry, vol. 86, no. 4, pp. 463–467, 1982.

[83] H. R. Gutiérrez, N. Perea-López, A. L. Elías, A. Berkdemir, B. Wang, R. Lv, F. López-Urías, V. H. Crespi, H. Terrones, and M. Terrones, “Extraordinary Room-Temperature

Photoluminescence in Triangular WS2 Monolayers," *Nano Letters*, vol. 13, no. 8, pp. 3447–3454, 2012.

[84] S.-H. Li, W. Yang, Y. Liu, X.-R. Song, R. Liu, G. Chen, C.-H. Lu, and H.-H. Yang, "Engineering of tungsten carbide nanoparticles for imaging-guided single 1,064 nm laser-activated dual-type photodynamic and photothermal therapy of cancer," *Nano Research*, vol. 11, no. 9, pp. 4859–4873, 2018.

[85] W. Feng, R. Wang, Y. Zhou, L. Ding, X. Gao, B. Zhou, P. Hu, and Y. Chen, "Ultrathin Molybdenum Carbide MXene with Fast Biodegradability for Highly Efficient Theory‐Oriented Photonic Tumor Hyperthermia," Advanced Functional Materials, vol. 29, no. 22, p. 1901942, 2019.

[86] "Reduced graphene oxide," *Graphene Info*, 05-Apr-2021. [Online]. Available: https://www.graphene-info.com/reduced-graphene-oxide-introduction. [Accessed: 28-Jun-2021].

[87] "Transition metal dichalcogenide monolayers," *Wikipedia*, 05-Jun-2021. [Online]. Available: https://en.wikipedia.org/wiki/Transition_metal_dichalcogenide_monolayers. [Accessed: 28-Jun-2021].

[88] "MXenes," *Wikipedia*, 14-Jun-2021. [Online]. Available: https://en.wikipedia.org/wiki/MXenes. [Accessed: 28-Jun-2021].

[89] T. Bao, X. Peng, W. Yin, and J. Lin, "Chemical Exfoliating 2D Molybdenum Oxide Nanoflakes for Cancer Cells Photothermal Ablation," *International Journal of Science*, vol. 3, no. 6, Jun. 2016.

[90] K. H. Ibrahim, M. Irannejad, B. Wales, J. Sanderson, K. P. Musselman, and M. Yavuz, "The Effect of Varying Ultrafast Pulse Laser Energies on the Electrical Properties of Reduced

Graphene Oxide Sheets in Solution," *Journal of Electronic Materials*, vol. 47, no. 2, pp. 1117–1124, 2017.

[91] Y. Gao, W. Huang, C. Yang, Z. Liu, H. Meng, B. Yang, Y. Xu, and C. Guo, "Targeted photothermal therapy of mice and rabbits realized by macrophage-loaded tungsten carbide," *Biomaterials Science*, vol. 7, no. 12, pp. 5350–5358, 2019.